Two raft wave energy converters a combined analysis on the optimisation of annual energy conversion and energy stability

Technical University Delft

Thomas Kluwer:
Student number: 4465792
Thesis committee:
O. Colomes
R. Gomes
A. Antonini

March 2, 2023

Abstract

Global warming has caused an increasing demand for renewable energy. Currently, 50% of the renewable energy is provided by wind and solar combined. However, these renewable energy sources are highly volatile. Wave energy converters can provide a stable renewable energy source. Previous research has contributed to understanding various combined effects of length, aspect ratio, hydro-elasticity and PTO damping on the optimisation of peak power absorption for regular waves. However, research on optimising the combined effects on annual energy production and especially power stability is missing. This thesis aims to better understand these effects by answering the following research question: "How can the combined effects of total length, aspect ratio, raft stiffness and PTO damping influence yearly energy conversion and energy stability of a pitching raft WEC"

To do this, a novel formulation for a monolithic finite element model containing Timoshenko beam theory and Linear potential flow is developed. This FEM consists of a two-dimensional domain, where the water is excited by linear irregular waves. The wave energy converter is modelled as two floating Timoshenko beams connected by a damped joint. The model is verified by proving that the solution converges according to the polynomial order +1 for decreasing mesh size. Additionally, it is proven that energy is conserved which shows that there is no wave reflection resulting from the domain boundaries. Finally, the model is validated by comparing the results of the structure with and without joint to previous research.

Two experiments are developed to understand the combined effects. Initially, an eigenmode analysis of the undamped structure is performed. This gives insight into the influence of individual parameters on the eigenfrequencies and shapes. Moreover, the real eigenmodes are used to decompose the real part of the complex resonance shapes of the relative rotation response amplitude operator (RAO). This provides a coupling between the performance according to the relative rotation RAO and the eigenmodes and frequencies. A limitation of this method is that phase differences cannot be considered.
The second experiment maximises the annual energy conversion and energy stability of the wave energy converter with three sets of variable parameters: (total length, aspect ratio, damping parameter), (total length, symmetrical raft stiffness, damping parameter) and (stiffness fore-aft, stiffness aft-raft, damping parameter). This is done in three steps. First, the RAO for the relative rotation at the joint is constructed. This is converted to a power spectrum. Secondly, the power spectrum is scaled by the JONSWAP energy density spectra. These spectra are constructed using the annual wave conditions, significant wave heights and peak periods from a wave scatter diagram. Subsequently, the results per spectrum are scaled by the number of occurrences of the wave conditions to obtain the annual energy conversion. Third, The optimum damping parameter per configuration is determined by calculating the annual energy conversion for a set of damping parameters. These results are interpolated to select the damping parameter that maximises annual energy conversion.
Finally, the performance of each configuration with their respective optimum damping parameter is assessed on annual energy conversion and capture width per peak wave period to give insight into the energy conversion and stability. The optimisation results are clarified with the results of the eigenmode analysis.

It was found that the optimal total length, considering raft stiffness, aspect ratio and PTO damping can be determined by matching the dimensionless wavelength corresponding to the third mode, and the annual significant wavelength.
Furthermore, It is proven that an aspect ratio of 0.2 to 0.3 increases the performance in high-frequency waves without compromising on low-frequency waves. The capture width is more evenly distributed over peak wave periods, indicating a higher energy stability. This results in an increase of annual energy conversion of 31% with respect to an aspect ratio of 0.5.
Besides the aspect ratio, it was found that an asymmetrical raft stiffness, with a moderately flexible fore raft and a rigid aft-raft increase energy stability without compromising annual energy conversion.

Preface

My optimism, and possibly naivety, have often led me to plan beyond the achievable. At the start of my thesis, I wanted to research fluid-structure interaction with an application that could contribute to society. I started with the plan to optimise wave energy converters considering hydro elasticity using a genetic algorithm for non-linear regular and linear irregular waves. Along the route, a continuous process of adjusting and refining led me to this final report. The grind of the thesis led me to repeat the mantra:

"Do you really want it to be easy"

This thesis concludes my study as a hydraulic engineer at the TU Delft. I will cherish my time in Delft. My study has given me the mathematical and physical skills an engineer needs while providing new facets for creative problem-solving.

The creation of this thesis could not have occurred without the love and support of my friends, family and partner, who have provided me with love and distraction when needed. I want to express my gratitude to all of them for being there. Also, I would like to thank my fellow students, who gave me feedback and support. Furthermore, I could not have fulfilled this thesis without the direction and input provided by my thesis committee.

Finally, I would like to express special thanks to two individuals. First of all, my fellow student and friend Dorette Regoutte, who has laid the groundwork for my thesis with her research on "hydro-elasticity of a multi-module, very large floating structure", and who has given me support and in-depth feedback whenever I asked. Secondly, I would like to thank Oriol Colomes, my supervisor, who has provided the guidance I needed throughout my thesis. Oriol was there when I needed him, and I could not have wished for better supervision.

Contents

1

Introduction

The demand for an energy transition has grown greatly in recent years. The European green deal has set goals of cutting greenhouse gasses by 55% with respect to 1990 [1], with at least 40% renewable energy mix by 2030, and to be the first climate-neutral continent by 2050[2]. In 2020, wind, hydro and solar generated most energy from renewable sources with 36%, 33% and 14% respectively (the remaining 16% comes from alternative sources). The advantage of these three power sources is they are well-proven technologies with a high return on investment [3]. However, these power sources have a significant environmental impact [4], putting pressure on land and water resources [5]. Furthermore, solar and wind are highly volatile power sources which depend on local weather conditions [6]. Hydropower is considered a stable energy source, and can even be used to store energy. However, it is highly dependent on geographical altitude differences and not suitable for low-lying countries like The Netherlands. Therefore, the energy supply is currently stabilised by non-renewable energy sources like gas and coal plants. In order to obtain a 100% renewable energy mix by 2050, diversifying the energy mix by adding more stable power sources is essential.

An alternative to wind and solar can be wave energy. The global wave energy is estimated at 2.11 ± 0.05 TW, of which 4.6% is extractable assuming an illustrative wave energy converter (WEC), (Pelamis P2) [7]. The distribution of this energy can be seen in figure 1.1. This makes wave power the highest density power source among renewable energy sources [8, 9]. Other advantages of wave power are its limited environmental impact and increased stability as a power source (wave power is available 90% of the time, whereas solar and wind are present only 20 - 30% of the time at a given site [9, 10]). To compete with wind and solar, increasing stability can play a key role. Therefore, maximising the annual energy conversion while stabilising the energy output will be this thesis's main goal.

1.1. Literature review

The idea of converting wave energy into electricity is not a new idea. The first patent was filed in 1790 [8]. However, the application of wave energy converters has never reached the level of cost competitiveness with conventional systems such as offshore wind or Photovoltaic cells. MacGillivray et al. [3] performed a learning investment sensitivity analysis. They showed that if wave energy converters are ever to compete with more mature technologies such as offshore wind or solar it is essential that the starting cost, learning rate, and capacity at which sustained cost reduction occurs need to be improved. The starting costs can be reduced by integrating WEC systems into other emerging technologies such as floating solar, very large floating structures or floating breakwaters. Increasing the learning rate requires the convergence of technologies. This absence of convergence is where wave energy converters differ from conventional renewables. For example, wind energy reached a convergence of designs with 3-blade rotors, positioned vertically, upwind of the support structure. This allows for more cost-effective optimisation and consequently scaling to reduce costs. Currently, a wide variety of wave energy converters exists, subdivided into three functioning mechanisms: oscillating water columns, over-topping devices and oscillating bodies, see figure 1.2. Therefore, optimising existing and mature technologies is preferable for the development of wave energy converters. In addition to reducing costs and increasing returns, addressing a different market can also increase the competitiveness of WEC. A problem that conventional renewables fail to solve is energy stability. G. Sokhna Seck et al. [11]

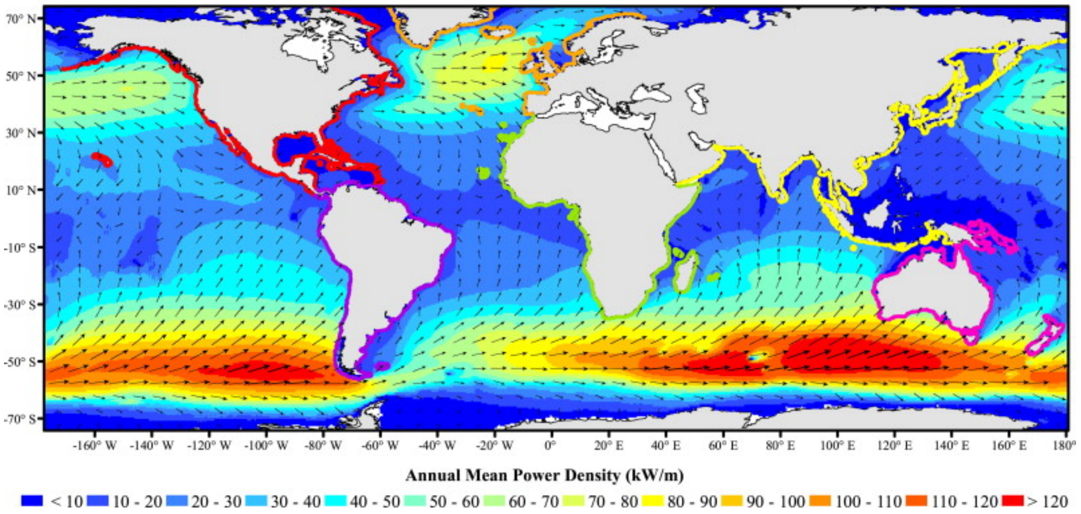

Figure 1.1: Annual mean wave power density (colour) and annual mean best direction (→). The land buffers used to quantify the resource are also shown, coloured by continent [7]

performed an analysis of the grid systems adequacy and transient stability in France. They showed that a maximum of 65% variable renewable energy can be installed for a reliable grid, leaving a 35% gap with the EU 2050 goals [2]. Because of the reasons mentioned above, this research will focus on pitching rafts wave energy converters, a mature technology that can be integrated and scaled.

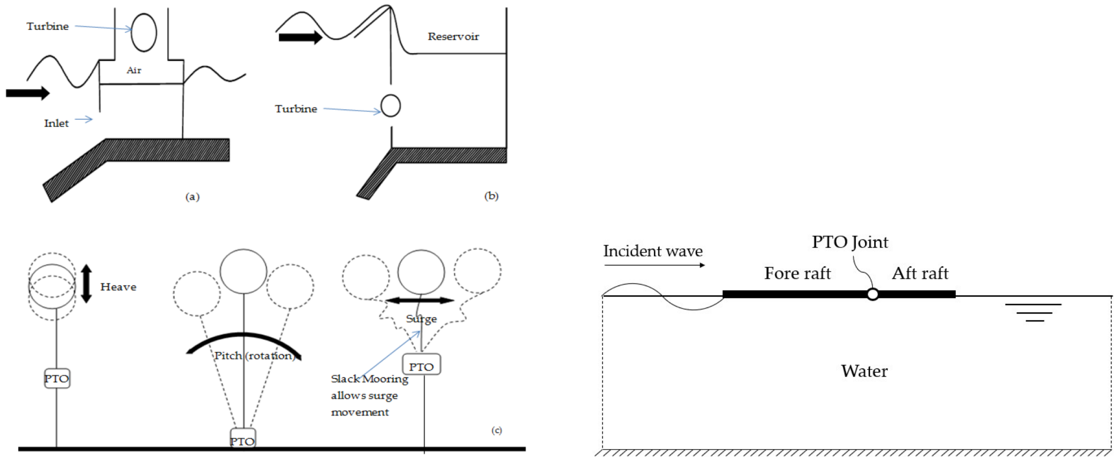

(a) Different types of WECs [12]

(b) General layout of a two-body pitching raft WEC

Figure 1.2: Wave energy converter types

The research into pitching raft WECs has moved in cycles, but in the 1970s, a new rise in research was driven by the oil crises [12, 13]. An early work that looked into the multi-body pitching rafts was performed by P. Haren [14]. P. Haren investigated the influence of varying lengths, PTO damping parameters and the number of rafts on the energy conversion for regular and irregular waves. The WEC parameters were optimised to maximise peak performance per frequency. Since then S.M. Zheng et al. [15] performed a numerical study considering three-dimensional wave diffraction-radiation theory for regular waves. In which they looked into the influence of both linear and coulomb PTO damping parameters, the radius of gyration, and axis ratio of an elliptical cross-section on the wave energy capture factor per frequency. They revealed a nonlinear relation between the optimal linear joint damping and the wave number. Furthermore, they have proven that the maximum power capture factor is the same for linear damping as for Coulomb damping when optimising for peak performance in regular waves.

Later on, S.M. Zheng et al. [16] constructed an analytical approach to optimise the damping parameter and stiffness of the PTO system, combined with the mass moment of inertia around the PTO system for peak per-

formance in regular waves. They showed that for general wave conditions and a specified total length for the WEC, a shorter fore raft compared to the aft raft can increase power absorption. Whereas for longer wavelengths, floats with equal lengths perform better.
In all the research mentioned above the raft is assumed to be fully rigid and hydro-elastic mechanisms are neglected. D. Lu et al. [17] looked into the combined effects of length ratios and structural flexibility on power capture performance for a two-raft WEC with a fixed length of 40m. This was done using a discrete-module-beam-bending-based hydroelasticity method derived by [18, 19] to derive the equations of motion. This method relies on subdividing the raft in freely floating discrete rigid elements with lumped mass, interconnected by rotational joints, of which the joint stiffness approaches the bending stiffness. The number of elements depends on the length and the ratio of the rafts, but a maximum of 8 elements was used. They concluded that for peak performance in regular waves: "Two rafts with identical length may be the optimal condition for power absorption in relatively long waves while the performance is weakened by increasing the structural flexibility of two rafts" and "Both the decrease of the fore-aft raft length ratio and the increase of structural flexibility lead to increase of power absorption in a shorter wave condition."
Crucial in all the before mentioned research is that the optimisation is performed for regular waves, and a comparison is made between the optimal configuration for each wavelength/period. WECs are designed solely for peak performance, ignoring the stability of the energy. The effect of irregular waves on power stability has been investigated by Y. Fu et al. [20], who considered non-linear joint damping for regular and irregular waves in the time. They showed that a nonlinear stiffness can shift the resonance peak to a lower frequency and play an important role in the phase control of the efficiency enhancement. More importantly, they showed that the peak value for a nonlinear system of the capture width can be almost double that of a linear system for irregular waves, adding a crucial distinction to the results found by [15]. This shows the importance of considering irregular waves when assessing WEC performance.

The previous research has contributed to the understanding of various combined effects of hydro elasticity, length ratio and PTO damping and stiffness of WEC design for regular waves. D. Lu et al. [17] have shown the influence of hydroelasticity on peak performance, and have proven that flexible fore rafts increase the power absorption for higher frequencies. Furthermore, the effect of WEC dimensions, PTO damping and draft have extensively been researched for irregular waves with various wave spectra. Nevertheless, no research has been done on the combined optimisation of total length, aspect ratio, raft stiffness and PTO damping for the annual energy conversion and energy stability of a pitching raft WEC.

1.2. Thesis outline

This section expands the thesis outline. The section starts with the problem statement, followed by the research question. Next, the scope of the thesis is described. Finally the report structure is presented.

1.2.1. Problem statement

The literature above shows that there is a need for stable energy sources [11] if a %100 renewable energy mix is to be achieved [2]. Wave energy conversion could solve part of this problem, with a source stability of that is present 90% of the time by [9, 10]). Length ratios and variable stiffness can shift the peak performance frequency and increase power absorption for higher frequencies [16, 17]. Yet, research on the energy stability of pontoon-type pitching rafts is limited.

1.2.2. Research question

To gain a better understanding of the influence of the combined effects of WEC dimensions, hydroelasticity and PTO damping on the optimisation of energy conversion and stability the following research question is examined:

- "How can the combined effects of total length, aspect ratio, structural stiffness and PTO damping influence yearly energy conversion and energy stability of a pitching raft WEC?"

The following subquestions have been posed to answer the research question.

- What are the individual effects of total length, aspect ratio and structural stiffness on the eigenfrequencies and corresponding dimensionless wavelengths?
- How do total length, aspect ratio and structural stiffness influence the eigenmode shapes?

- What is the influence of the first ten eigenmodes on resonance peaks of the RAO?
- How can total length, aspect ratio, raft stiffness and PTO damping be optimised to maximise annual energy conversion and stability?
- What is the relation of total length, aspect ratio, raft stiffness and PTO damping to one another when maximising annual energy conversion and stability?

1.2.3. Scope

The research focuses on the hydrodynamics of a pitching raft WEC excited by irregular waves. The focus will be on the influence of total length, aspect ratio, hydroelasticity and PTO damping, and their combined effects. The motion of the structure and the fluid will be assessed using a novel formulation for a monolithic FEM containing Timoshenko beam theory and Linear potential flow. The results will be clarified by an eigenmode analysis.

The structure is modelled as two floating Timoshenko beams with uniform cross-sections, mass and stiffness. The rafts are joined by a dimensionless and mass-less PTO system simulated as a damped joint. The fluid is modelled using linear potential flow theory. Furthermore, the system is excited by regular waves. The response can be scaled according to the random phase amplitude model by a JONSWAP energy density spectrum. The structure's performance is assessed on annual energy conversion and capture width over various mean wave periods based on results in the frequency domain. To assess all of the above, a 2-dimensional model is created in Gridap [21, 22], a finite element package in the programming language Julia.

The topics that are explicitly not within the scope of this thesis are the following. Therefore, electrical systems and their efficiency are not included in this research, nor is a reduction parameter for electrical efficiency. Furthermore, no motion constraints are considered. Large relative rotation can lead to collision and damage. This thesis primarily focuses on exploring the influence of hydroelasticity on hydrodynamic efficiency and power capacity and therefore neglects motion constraints.

1.2.4. Report structure

The report structure is shown in figure 1.3. The report starts with a theoretical basis. Elaborating on the experimental setup, the formulations used to model the structure and fluid behaviour, the wave conditions, the frequency domain and the optimisation of the WEC parameters.

Following this is the chapter containing the numerical formulation. This chapter focuses on the implementation of the theory into a numerical framework. It expands the weak form and shows the validation and verification of the numerical model.

Chapter 4 reports and discusses the results. It starts with an eigenmode analysis to give insight into the influence of individual parameters on the WEC behaviour. Consequently, these eigenmodes are used to decompose the resonance shapes from the RAO. Finally, an optimisation for annual energy conversion and energy stability shows the coupled effect of three sets of variable parameters, namely, the total length, aspect ratio and damping coefficient $[L_{tot}, \alpha_l, \overline{c}_r]$, the symmetric stiffness, aspect ratio and damping coefficient $[\overline{E}, \alpha_l, \overline{c}_r]$ and the asymmetric stiffness and damping coefficient $[\overline{E}_1, \overline{E}_2, \overline{c}_r]$.

A conclusion is presented in chapter 5, summarising the findings.

Chapter 6 discusses the limitations of this research and poses recommendations for future research.

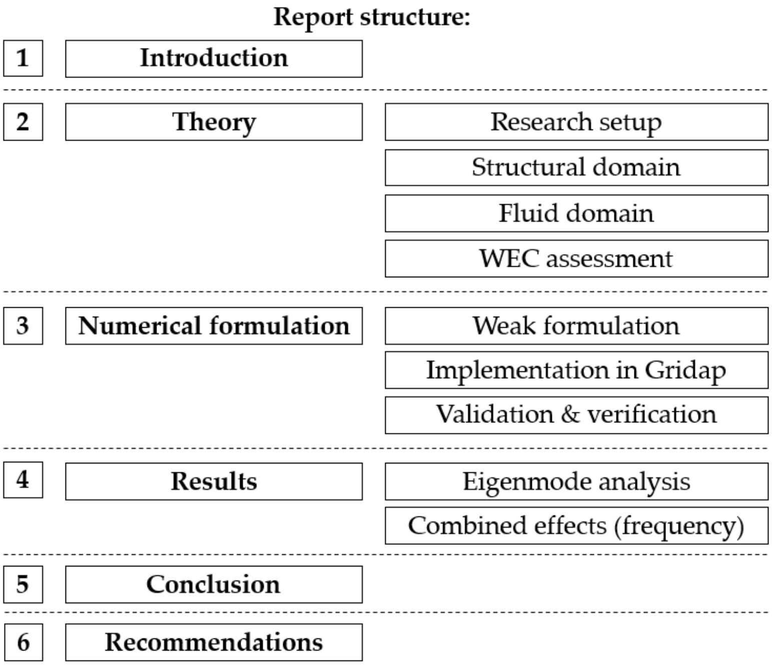

Figure 1.3: Thesis outline

2

Theory

This chapter explains the theoretical basis. The chapter starts with a description of the research setup. consequently, it defines the analytical equations for the structural and fluid domain. This contains the equations of motion, boundary and interface conditions and the damping zones. The next section elaborates on the linear wave formulation for regular and irregular waves. Subsequently, the theory valid in the frequency domain is elaborated, including information about the method used to obtain eigenfrequency and mode shapes. Finally, the chapter concludes with the WEC optimisation and assessment.

2.1. Research set-up

This research aims to investigate the combined effects of hydro-elasticity, length, aspect ratio and PTO damping on the energy conversion and energy stability of a WEC. To do so, a two-body raft is modelled in a two-dimensional numerical wave tank. The water is modelled using linear potential flow theory, which states that the fluid is incompressible, irrotational and inviscid. On either end of the model, a damping zone is present to eliminate reflection from the vertical boundaries.

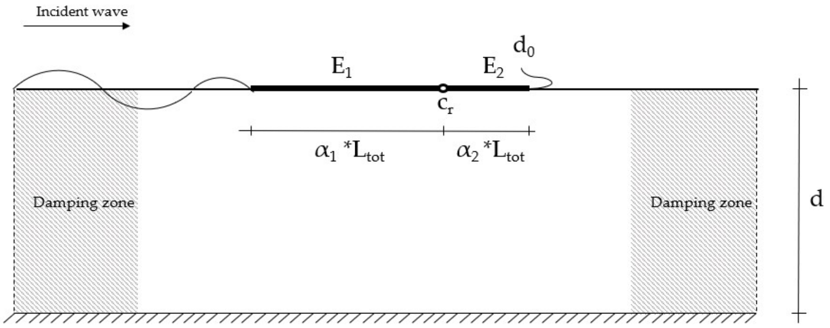

Figure 2.1: Overview of model and parameters of interest

E : raft stiffness c_r : PTO damping

d_0 : draft d : depth α : aspect ratioL_{tot} : Total length

The WEC is modelled as 2 floating flexible beams with a uniform cross-section, mass and stiffness, modelled by the Timoshenko beam equations. For a Timoshenko beam-like flexible structure, the stiffness is governed by the bending stiffness (EI) while considering shear deformation (kAG). The bending stiffness is dependent on Young's modulus (E) of the material and the cross-section area moment of inertia (I). Note that changing Young's modulus has the same effect as changing the moment of inertia. For this research, the stiffness is varied by altering the young modulus E for a constant moment of inertia I = 3.588 m ^{4}. Therefore, Young's modulus will also be referred to as the stiffness coefficient. This moment of inertia is chosen for a solid ellipsoidal cross-section $I = \frac{1}{64}ab^3$ equal to [17]. Furthermore, the shear deformation is neglected by enforcing a slenderness criterium, making the shear modulus dependent on Young's modulus. The beams are connected by a joint which contains the PTO system, modelled as a damped joint. The dimensions of the rafts are governed by the total length of the WEC L_{tot}, and the aspect ratios α_l. The dimension of the PTO joint is neglected, meaning that no free surface of the water is present between the two bodies. Furthermore, there is no collision constraint at the joint, meaning that $\Delta\theta$ is unlimited. Finally, the mass of the rafts is indicated by the draft of the structure. The PTO is assumed to have no mass.

The WEC is forced by a linear regular wave with unit amplitude. The response to irregular waves is determined by scaling the power spectrum with the energy density spectrum of irregular waves. Furthermore, the annual energy conversion is calculated by connecting the JONSWAP spectrum with a wave scatter diagram, containing the mean zero-crossing periods T_{av} and the significant wave heights H_s and their respective number of occurrences.

To assess the performance of WECs the energy conversion is judged on the following performance indicators:

- Annual converted energy E_{tot}
- Normalised Annual converted energy E_{tot}/L_{tot}
- Capture width $CW(T_{av})$
- Power spectrum

Initially, the WECs are exposed to a set of regular waves in the frequency domain to construct the Response Amplitude Operator (RAO) for the relative rotation. The RAO is converted into a power spectrum. Consequently, this is used to calculate the half-hourly energy and annual energy by the procedure described in 2.6. Finally, the response in the frequency domain is assessed on the annual energy conversion, normalised capture width and power spectrum.

All of the above is tested by means of a numerical simulation. A novel formulation for a monolithic finite element model containing Timoshenko beam theory and Linear potential flow is developed. To do this the FEM library Gridap [21], [22] is utilised. Gridap requires the formulation of a weak form and provides tools such as mesh and matrix constructors and solvers.

2.2. Structural domain

The structural domain refers to the two rafts and the PTO joint that compose the WEC. The equations of motion of the structure will be treated in subsection 2.2.1. Subsequently, The interface conditions occurring at the joint are treated in subsection 2.2.2.

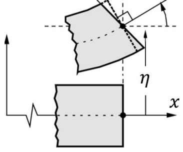

Figure 2.2: Variable definition for Timoshenko beam

2.2.1. Structural equations of motion

The structural domain considers the rafts and the PTO, which are modelled as 2 Timoshenko beams connected by a damped and stiff joint. The Timoshenko beam theory does not assume that the cross sections perpendicular to the beam axis remain perpendicular, see figure 2.2. The reason the Timoshenko beam formulation is chosen is twofold. Primarily, applying the Timoshenko beam formulation enables the numerical formulation to be constructed in a more direct manner, avoiding the need for penalty terms in the Hermite shape functions. Secondly, the Timoshenko beam formulation allows for the inclusion of shear deformation, and using this formulation creates a more versatile model. Nonetheless, the influence of shear deformation is not considered in this phase of research, to keep the number of free variables manageable. The Timoshenko beam formulation is defined in equations (2.1) and (2.2).

$$\rho A\frac{\partial^2\eta}{\partial t^2} = kGA\left(\frac{d\eta^2}{dx^2} - \frac{d\theta}{dx}\right) + p \tag{2.1}$$

$$\rho I\frac{\partial^2\theta}{\partial t^2} = EI\frac{d\theta^2}{dx^2} + kGA\left(\frac{d\eta}{dx} - \theta\right) \tag{2.2}$$

ρ : density beam A : cross sectional area η : deflection t : time
k : shear area coefficient G : shear modulus θ : rotation p : External pressure
E : Youngs modulus I : Cross sectional moment of inertia L : Beam length

In order to neglect the shear deformation the shear stiffness is directly dependent on the bending stiffness by imposing the slenderness criteria formulated in equation (2.3).

$$\frac{kGAL^2}{EI} = 10.000 \tag{2.3}$$

This method results in a formulation that approaches the Euler-Bernoulli formulation while maintaining the versatility of the Timoshenko formulation for future research.

2.2.2. Interface conditions

The interface conditions provide the coupling of the two rafts. The rafts are connected via a rotational joint. No translational motion is allowed in the joint, which results in a constant displacement and shear force along the joint, see equation (2.4) and (2.5).

$$\text{constant displacement}: \quad \eta_1^+ = \eta_2^- \tag{2.4}$$

$$\text{constant shear}: \quad kGA\left(\frac{\partial\eta_1}{\partial x} - \theta_1\right) = kGA\left(\frac{\partial\eta_2}{\partial x} - \theta_2\right) \tag{2.5}$$

Because the type of WEC considered is a pontoon-type pitching device, the energy extraction is performed via a PTO system in the joint. This is modelled as a linearly damped joint. The PTO system in the joint causes a moment, see equation (2.6) and (2.7).

$$\text{Damping moment}: \quad M_c = c_r\left(\frac{\partial\theta_1}{\partial t} - \frac{\partial\theta_2}{\partial t}\right) \tag{2.6}$$

$$\text{Constant moment}: \quad EI_1\frac{\partial\theta_1}{\partial x} = EI_2\frac{\partial\theta_2}{\partial x} = M_c \tag{2.7}$$

c_r : PTO damping M_c : Moment due to damping

The PTO stiffness is not considered in this research. Y. Zheng et al. [15] showed that PTO stiffness can only improve energy conversion in the case of non-homogeneous rafts with external mass, which is outside the scope of this research.

2.3. Fluid domain

The fluid domain consists of the water which is enclosed by the free surface, the structure interface, the incident vertical boundary, the outgoing vertical boundary and the bottom, see figure 2.3. The equation of motion and boundary conditions will be explained in subsections 2.3.1 and 2.3.2 respectively.

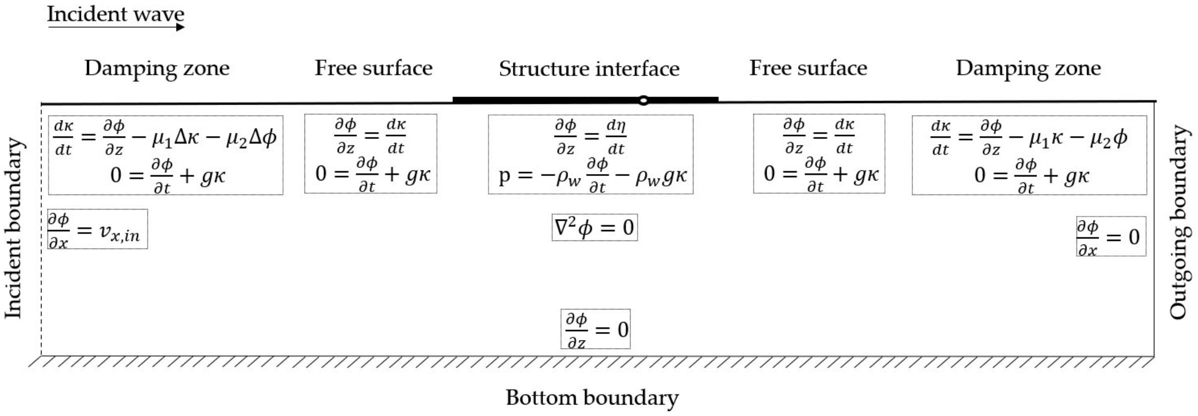

Figure 2.3: The fluid domain, including boundary conditions

2.3.1. Fluid equations of motion

The water is assumed to be incompressible, inviscid and irrotational. The velocity potential satisfies the linear potential flow theory by equation (2.8).

$$\nabla^2\phi = 0 \tag{2.8}$$

ϕ : velocity potential

The linear potential flow theory allows for the linearization of the Bernoulli, expressed as equation (2.9)

$$\frac{\partial\phi}{\partial t} + \frac{p}{\rho_w} + g\kappa = 0 \tag{2.9}$$

ρ_w : density water g : gravitational acceleration κ : free surface elevation

2.3.2. Boundary conditions

The boundary conditions dictate the behaviour of the water at the boundaries of the domain. The fluid domain boundaries can be separated into 5 sections. From top to bottom, the free surface, the structure interface, the incident boundary, the outgoing boundary and the bottom surface.

The free surface contains a kinematic and a dynamic boundary condition. The dynamic boundary condition is given by the Bernoulli equation for unsteady flow shown in equation (2.9), with the pressure term equal to zero at the free surface. The kinematic boundary condition states that the velocity normal to the water surface is equal to the speed with which the water surface rises and falls. This results in the kinematic boundary condition (2.10) and the dynamic boundary condition (2.11).

$$\frac{\partial\phi}{\partial z} = \frac{\partial\kappa}{\partial t} \tag{2.10}$$

$$0 = \frac{\partial\phi}{\partial t} + g\kappa \tag{2.11}$$

Part of the surface is in contact with the structure. Similar to the boundary conditions of the free surface this interface is dictated by a dynamic and kinematic boundary condition. However, the pressure term (p) in the Bernoulli equation is equal to the pressure exerted by the structure. This provides a coupling term between the structural equations of motion and the fluids equation of motion. This results in the kinematic boundary condition (2.12) and the dynamic boundary condition (2.13).

$$\frac{\partial\phi}{\partial z} = \frac{\partial\eta}{\partial t} \tag{2.12}$$

$$p = -\rho_w \frac{\partial \phi}{\partial t} - \rho_w g \eta \tag{2.13}$$

By applying these boundary conditions no separation of the structure and the surface is enforced
The vertical boundary where the wave enters the domain is called the incident boundary. By definition, the x-derivative of the velocity potential is equal to the horizontal velocity. The horizontal velocity $\mathrm{v_{x,in}}$ in this case, is dictated by the horizontal velocity of the wave. This results in equation (2.14)

$$v_{x,in} = \frac{\partial \phi}{\partial x} \tag{2.14}$$

$v_{x,in}$ = Horizontal wave velocity at incident boundary

The vertical boundary opposite the incident boundary is referred to as the outgoing boundary. However, in this wave tank, this is a closed boundary meaning there is no flow normal to the boundary. To avoid reflection at both vertical boundaries a damping zone is installed, see figure 2.3, which will be elaborated in subsection 2.3.3. A closed boundary results in no velocity normal to the boundary, see equation (2.15).

$$\frac{\partial \phi}{\partial x} = 0 \tag{2.15}$$

The bottom of the domain is considered to be impermeable, e.g. no fluid enters or exits through the bottom. Therefore, the vertical velocity is equal to zero, resulting in equation (2.16)

$$\frac{\partial \phi}{\partial z} = 0 \tag{2.16}$$

2.3.3. Damping zone

In order to avoid reflection of the waves at the domain boundary, a damping zone is included, see figure 2.3. Reflection of the waves may lead to energy accumulation and a numerically unstable model. In this research, the artificial beach method is used, which consists of two elements. The first element is the damping coefficient which determines the maximum strength of the damping zone. Secondly, the shape function determines the transition from zero to the maximum damping coefficient.

Kim et al. [23] compared five methods, damping the following components:

1. The surface velocity [ϕ_n]
2. The velocity potential [ϕ]
3. The velocity potential and surface velocity [$\phi;\phi_n$]
4. The surface elevation and the velocity potential [$\kappa;\phi$]
5. The surface velocity and the surface elevation [$\phi_n;\kappa$]

These five methods were each combined with four different shape functions. Their study showed that the fourth method [$\eta;\phi$] and the fifth method [$\phi_n;\kappa$] perform best by limiting energy accumulation in the model. In contrast to the fifth method, the fourth method is independent of the wave number to enforce no dispersion and distortion, which is required for the damping of irregular waves. The fourth method used the dynamic and kinematic free surface condition shown in the linearised equations (2.17), (2.18) respectively.

$$\frac{\delta \phi}{\delta t} = -g\kappa \tag{2.17}$$

$$\frac{\delta \kappa}{\delta t} = \frac{\partial \phi}{\partial z} - \mu_1 \kappa - \mu_2 \phi \tag{2.18}$$

The damping terms μ_1 and μ_2 are a combination of the damping coefficient μ_0 and the shape function. The velocity potential damping (μ_2) is related to surface elevation damping (μ_1) to enforce no distortion or dispersion. The damping terms μ_1 and μ_2 are given by equation (2.19) and (2.20).

$$\mu_1(x) = \mu_0 \left[1 - \cos\left\{\frac{\pi}{2}\left(\frac{x - x_d}{l_d}\right)\right\}\right] \tag{2.19}$$

$$\mu_2 = -\frac{\mu_1^2}{4} \tag{2.20}$$

l_d : Damping zone length x_d : x-coordinate start damping zone

The governing parameters for the damping terms are the damping strength μ_0 and the length of the damping zone l_d. Both of these parameters depend on the wave properties, where μ_0 should exceed the critical damping, and l_d should at least be equal to the characteristic wavelength [24]. However, due to the nature of irregular waves, the wave frequency and length vary. Therefore a combination of the damping coefficient and damping zone length needs to be chosen, such that the reflection is avoided while minimizing the computational domain. Equations (2.21) by Kim et al [24] are used as a starting point.

$$\mu_0 > 1.25\mu_c \qquad \mu_c = 2\omega_p \tag{2.21}$$

ω_d : peak angular frequency l_d : length damping zone λ_p : peak wavelength

Finally, a damping length l_d = 30 and a peak angular frequency of ω = 0.82 are chosen. The verification of these parameters is shown in section 3.2. At the incident boundary, reflection has to be avoided without damping the incident waves. This is done by damping only the reflected surface elevation (κ) and velocity potential (ϕ), see the linearised equations (2.22), (2.23)

$$\frac{\delta\phi}{\delta t} = -g\kappa \tag{2.22}$$

$$\frac{\delta\kappa}{\delta t} = \frac{\partial\phi}{\partial z} - \mu_1(\kappa - \kappa_{in}) - \mu_2(\phi - \phi_{in}) \tag{2.23}$$

κ_{in} : surface elevation incident boundary ϕ_{in} : Velocity potential incident boundary

2.4. Linear waves

This section describes the linear wave theory. The section will initiate with the formulation of linear regular waves, followed by the description of irregular waves.

2.4.1. Regular waves

Linear wave theory provides a linearised solution for propagating harmonic waves. based on the assumptions that the fluid is incompressible, irrotational and inviscid. The wave equation for linearised regular waves consists of a velocity potential and a surface elevation. The solutions result from the linearised mass and momentum balance. These equations give rise to the linearised Bernoulli equation which at the surface level states that the surface elevation is equal to the time derivative of the velocity potential, as was shown in equation (2.11). The velocity potential and surface elevation for linear waves are formulated in equations (2.24) and (2.25).

$$\phi_{in}(x,z,t) = \kappa_0 \frac{\omega}{k}\frac{\cosh(kz)}{\sinh(kd)}\sin(kx - \omega t) \tag{2.24}$$

$$\kappa_{in}(x,t) = \kappa_0 \cos(kx - \omega t) \tag{2.25}$$

κ_0 : wave amplitude k : angular wave number d : water depth

2.4.2. Irregular waves

The linear regular wave theory can be expanded for irregular waves by applying the random phase amplitude model. This model rests on the idea that the surface elevation and velocity potential for irregular waves are the sum of a large number (N) of harmonic waves. Consequently, the response of the structure to irregular waves can be modelled as a linear superposition of the response to regular waves. The formulation of the random phase amplitude model is presented in equation (2.26).

$$\kappa(t) = \sum_{i=1}^{N} \underline{a}_i \cos\left(2\pi f_i t + \alpha_i\right) \tag{2.26}$$

a_i : wave amplitude f : wave frequency α_i : phase difference

For each frequency, the phase is drawn from a uniform distribution $[0, 2\pi]$. The amplitude results from the wave amplitude spectrum. In this research, the JONSWAP frequency spectrum is used as a basis for this amplitude spectrum [25]. The JONSWAP spectrum is valid for timescales in the order of half an hour up to an hour. The formulation of the spectrum is presented in equation (2.27).

$$S_{\text{JONSWAP}}\left(f\right) = \alpha g^2 (2\pi)^{-4} f^{-5} \exp\left[-\frac{5}{4}\left(\frac{f}{f_{\text{peak}}}\right)^{-4}\right] \gamma^{\exp\left[-\frac{1}{2}\left(\frac{f/f_{\text{peak}}-1}{\sigma}\right)^2\right]} \tag{2.27}$$

The annual wave climate is presented in a wave scatter diagram, listing combinations of significant wave height and period, and their respective number of occurrences. By reformulating equation (2.27) in terms of significant wave height and peak wave period, the corresponding wave spectra can be obtained. This is done according to Goda et al. [26] in equation (2.28).

$$S(f) = \beta_j H_s^2 T_p^{-4} f^{-5} \exp\left[-\frac{5}{4}\left(T_p f\right)^{-4}\right] \gamma^{\exp\left[\frac{-(T_p f-1)^2}{2\sigma}\right]} \tag{2.28}$$

H_s : significant wave height T_p : peak wave period γ : peak enhancement function
σ_a : shape function σ_b : shape function

Three constants adjust the JONSWAP spectrum, namely the peak enhancement factor $\gamma = [1:7]$, and the shape functions σ_a, σ_b, which are dependent on the location. β_j is a scaling factor of the peak enhancement factor γ, see equation (2.29).

$$\beta_j = \frac{0.0624}{0.230 + 0.0336\gamma - 0.185(1.9+\gamma)^{-1}}\left[1.094 - 0.01915 \ln\gamma\right] \tag{2.29}$$

To specify an annual wave climate the Atlantic marine energy test site(AMETS) off Belmullet, Co. Mayo, Ireland is chosen as a representative testing site. The wave climate at AMETS is chosen because it is a frequently used test site for WECs in moderate to deep water conditions. It possesses a favourable wave climate and the required infrastructure. Goggins et al. [27] presented a wave scatter diagram for 2011, see figure 2.4. The year 2011 is chosen because Goggins et al. [27] have shown that this is a representative year with representative wave conditions. To obtain the data in figure 2.4 a Fugro Wavescan buoy is used to record the real-time wave data which is located approximately 3 km offshore at a water depth of 50 m. The measured wave records are taken over a half-hour time frame.

Mazarreto et al. [28] performed a global evaluation of the JONSWAP spectrum for coastal areas. They used hindcast data and compared this with 39 wave buoys for areas worldwide. They found that the best fit for the AMETS location is obtained for the constants shown below:

$\gamma = 1.5$ $\sigma_a = 0.07$ $\sigma_b = 0.09$

The JONSWAP formulation proposed allows setting a JONSWAP spectrum for a specific significant wave height and peak period. Therefore, the zero mean crossing period presented in figure 2.4 needs to be converted to a peak period. Gode et al. [26] provided an equation converting the significant wave period to peak period shown in equation (2.30).

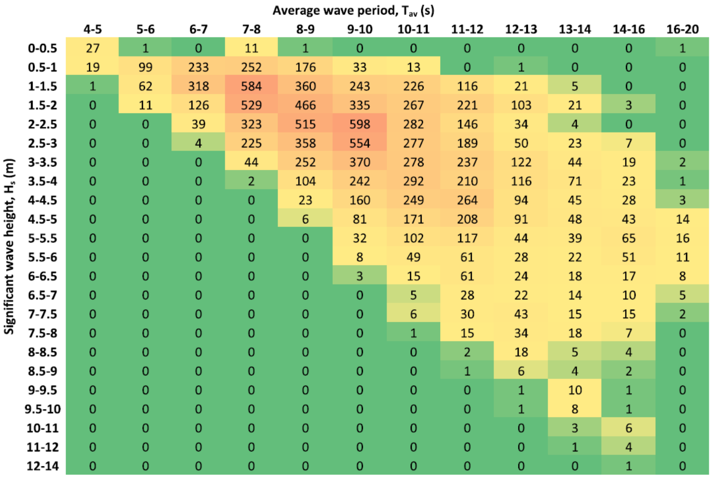

Significant wave height, H_s (m)	Average wave period, T_{av} (s)											
	4-5	5-6	6-7	7-8	8-9	9-10	10-11	11-12	12-13	13-14	14-16	16-20
0-0.5	27	1	0	11	1	0	0	0	0	0	0	1
0.5-1	19	99	233	252	176	33	13	0	1	0	0	0
1-1.5	1	62	318	584	360	243	226	116	21	5	0	0
1.5-2	0	11	126	529	466	335	267	221	103	21	3	0
2-2.5	0	0	39	323	515	598	282	146	34	4	0	0
2.5-3	0	0	4	225	358	554	277	189	50	23	7	0
3-3.5	0	0	0	44	252	370	278	237	122	44	19	2
3.5-4	0	0	0	2	104	242	292	210	116	71	23	1
4-4.5	0	0	0	0	23	160	249	264	94	45	28	3
4.5-5	0	0	0	0	6	81	171	208	91	48	43	14
5-5.5	0	0	0	0	0	32	102	117	44	39	65	16
5.5-6	0	0	0	0	0	8	49	61	28	22	51	11
6-6.5	0	0	0	0	0	3	15	61	24	18	17	8
6.5-7	0	0	0	0	0	0	5	28	22	14	10	5
7-7.5	0	0	0	0	0	0	6	30	43	15	15	2
7.5-8	0	0	0	0	0	0	1	15	34	18	7	0
8-8.5	0	0	0	0	0	0	0	2	18	5	4	0
8.5-9	0	0	0	0	0	0	0	1	6	4	2	0
9-9.5	0	0	0	0	0	0	0	0	1	10	1	0
9.5-10	0	0	0	0	0	0	0	0	1	8	1	0
10-11	0	0	0	0	0	0	0	0	0	3	6	0
11-12	0	0	0	0	0	0	0	0	0	1	4	0
12-14	0	0	0	0	0	0	0	0	0	0	1	0

Figure 2.4: Number of occurrences of significant wave heights and mean zero crossing periods at AMETS for 2011. [27]

$$T_p \simeq \frac{T_s}{1 - 0.132(\gamma + 0.2)^{-0.599}} \tag{2.30}$$

T_s : significant wave period

To derive the significant period from the zero mean crossing period the method of N. Nordenstorm et al. [29] is used in equation (2.31)

$$T_s = 2.83 T_{av}^{0.44} \tag{2.31}$$

T_{av} : mean zero crossing period

2.5. Frequency domain

The frequency domain allows for a computationally efficient assessment of dynamic systems. As mentioned earlier irregular waves can be modelled as a linear superposition of regular waves. Therefore the response per frequency can be scaled and summed, this method (spectral analysis) provides average performance results considering a large time interval. This section will initiate with a subsection on the response amplitude operator. Subsequently, the method used to obtain the eigenfrequencies and modes is discussed. Finally, the section finishes with the modal decomposition of resonance shapes.

2.5.1. Response Amplitude operator

The response of the structure for a unit amplitude per frequency can be collected in a response spectrum, this is also called a response amplitude operator. The response amplitude operator shows the amplitude of the parameter of interest, in this case, the relative rotation $\Delta\theta$ per frequency for a unit wave amplitude ($\kappa_0 = 1$). Consequently, the relative angular velocity $\Delta\frac{\partial\theta}{\partial t}$ RAO can be constructed from the relative rotation $\Delta\theta$ RAO using equation (2.32).

$$\Delta\frac{\partial\theta}{\partial t} = \Delta\theta f \tag{2.32}$$

$$\Delta\frac{\partial\theta}{\partial t} : \text{relative angular velocity} \qquad \Delta\theta : \text{relative angular displacement} \tag{2.33}$$

Because the system is linear, the response in the RAO can be scaled with the wave height. This allows the RAO to be scaled by a wave amplitude spectrum, which will be used for the optimisation presented in 2.6.

2.5.2. Eigen frequencies

The eigenfrequencies, or natural frequencies, are frequencies at which a system can vibrate without the presence of forcing. By tuning the system such that the eigenfrequencies lie close to the forcing frequencies, resonance occurs. This can be used to maximise energy conversion. The equations of motion derived in section 2.2 and 2.3 can be written in matrix notation splitting the structure and water. By doing this, one can avoid singularities when computing the eigenfrequency. This is represented in figure 2.5.

$$\begin{bmatrix} structure & coupling \\ coupling & water \end{bmatrix} \begin{bmatrix} structure \\ water \end{bmatrix} = \begin{bmatrix} Force_{structure} \\ Force_{water} \end{bmatrix}$$

Figure 2.5: Representation of the decoupling matrix

Before the terms are entered in this matrix, let's define the following notation.

S : Structure trail functions $(\eta, \theta_1, \theta_2)$	W : Water trial function (ϕ)
s : Structure test functions (v, z_1, z_2)	w : Water test function (w)

The definition of the test and trial functions will be provided in section 3.1. To construct the mass $\boldsymbol{M_{sS}}$, Damping $\boldsymbol{C_{sS}}, \boldsymbol{C_{sW}}, \boldsymbol{C_{wS}}$ and stiffness $\boldsymbol{K_{sS}}$ and $\boldsymbol{K_{wW}}$ matrices, the weak from presented in (3.40) is split into mass (acceleration dependent), damping (velocity dependent) and stiffness (displacement dependent) terms. Furthermore, the damping zones are omitted from the equations and considered free surfaces in the eigenfrequency analysis. The homogeneous mass, damping and stiffness equations are then transformed into matrices using a matrix constructor in Gridap.

Substituting the mass, damping and stiffness matrices results in equation (2.34).

$$\begin{bmatrix} [-\omega^2 \boldsymbol{M}_{sS} - i\omega \boldsymbol{C}_{sS} + \boldsymbol{K}_{sS}] & [i\omega \boldsymbol{C_{sW}}] \\ [-i\omega \boldsymbol{C_{wS}}] & [\boldsymbol{\hat{K}_{wW}}] \end{bmatrix} \begin{bmatrix} S \\ W \end{bmatrix} = \begin{bmatrix} F_S \\ F_W \end{bmatrix} \tag{2.34}$$

$\boldsymbol{M}$: mass matrix $\boldsymbol{C}$: damping matrix $\boldsymbol{K}$: stiffness matrix F : force

Note that the stiffness of the water $\boldsymbol{\hat{K}_{wW}}$ is a coupling matrix consisting of the hydro-static stiffness, and radiation damping. The latter couples the free surface to the water volume via radiation damping, resulting in a frequency dependent added mass term. The influence of this radiation damping is neglected in the eigenvalue analysis. $\boldsymbol{\hat{K}_{wW}}$ will therefore be referred to as $\boldsymbol{K_{wW}}$ for the remainder of this section.

$$\boldsymbol{\hat{K}_{wW}} = \boldsymbol{K_{wW}} + \omega^2 \boldsymbol{C_{wU}} \boldsymbol{K}_{uU}^{-1} \boldsymbol{C_{uW}} \tag{2.35}$$

U : free surface trail functions (κ)	u : free surface test function (u)

The second row of (2.34) can be rewritten isolating W this results in equation (2.36).

$$W = \boldsymbol{K}_{wW}^{-1}(F_W - i\omega \boldsymbol{C}_{wS} S) \tag{2.36}$$

Entering this expression for W in the first row of (2.34) results in the isolated problem (2.37).

$$\left(-\omega^2 \boldsymbol{M}_{sS} - i\omega \boldsymbol{C}_{sS} + \boldsymbol{K}_{sS} + \omega^2 \boldsymbol{C_{sW}} \boldsymbol{K_{wW}}^{-1} \boldsymbol{C_{wS}}\right) S = F_S + i\omega \boldsymbol{K_{wW}}^{-1} F_W \tag{2.37}$$

Note that implementing W in this manner gives rise to an additional ω^2 term which is another frequency-dependent added mass term. Consequently, (2.37) can be rewritten as equation (2.38).

$$\left(-\omega^2 (\boldsymbol{M}_{sS} - \boldsymbol{C_{sW}} \boldsymbol{K_{wW}}^{-1} \boldsymbol{C_{wS}}) - i\omega \boldsymbol{C}_{sS} + \boldsymbol{K}_{sS}\right) S = F_S + i\omega \boldsymbol{K_{wW}}^{-1} F_W \tag{2.38}$$

The first three terms can be combined in $\boldsymbol{\hat{M}}$, setting the forcing terms equal to 0 results in the homogenous equation (2.39).

$$-\omega^2\hat{\boldsymbol{M}} - i\omega\boldsymbol{C}_{sS} + \boldsymbol{K}_{sS} = 0 \tag{2.39}$$

Finally, the damping term $\boldsymbol{C}_{sS}$ results solely from the PTO damping. The PTO damping is omitted for the eigenshape analysis to allow for a real solution for the eigenfrequency analysis. The effects of neglecting the radiation and PTO damping will be discussed in the results, section 4. To calculate the eigen frequency of the undamped system, the determinant of the undamped system has to equal 0, as shown in equation (2.40).

$$\det[-\omega^2\hat{\boldsymbol{M}} + \boldsymbol{K}_{sS}] = 0 \tag{2.40}$$

For a n x n matrix, this results in n positive real eigenfrequencies.

2.5.3. Modal decomposition of resonance shapes

Modal decomposition of the resonance shapes refers to the decomposing of a resonance shape by eigenmodes and amplitudes. This can be done because the eigenshapes are orthogonal, which results in a modal amplitude for each eigenmode. Initially, the resonance shapes need to be determined, this can be done using the θ RAO. The θ RAO in figure 2.7a provides the relative rotation of the two rafts at the joint. The peaks in the RAO shown in figure 2.7a show the resonance frequencies. For these frequencies, there is a corresponding resonance shape in the frequency domain. The resonance shapes represent the complex maximum amplitudes. The complex amplitude can be separated into a real part and an imaginary part, representing the amplitude and phase difference respectively. The real component of the resonance shape is shown in figures 2.7b and 2.7c. Because the eigenmode analysis results in real orthogonal eigenshapes, shown in 2.6, these real resonance shapes can be decomposed into eigenmodes and respective amplitudes using equation (2.41).

$$\boldsymbol{E}a(f) = Re(x(f)) \qquad\qquad a(f) = \boldsymbol{E}^{-1}Re(x(f)) \tag{2.41}$$

$\boldsymbol{E}$: Eigen vector matrix $\qquad a(f)$: modal amplitude $\qquad x(f)$: resonance shape

The amplitude of each eigenmode indicates the presence of that mode in a specific resonance shape, shown in figure 2.7d. This provides a tool to assess the behaviour of the WEC. Primarily, the influence of individual parameters on the eigen shapes and frequencies can be coupled to the forced behaviour represented by the RAO. This coupling provides further verification of the behaviour. Moreover, it gives insight into the physical cause of the behaviour represented by the RAO.

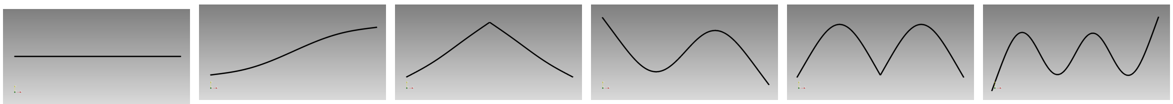

(a) f ≈ $0Hz$ (b) f = 0.103 Hz (c) f = 0.146 Hz (d) f = 2.07 Hz (e) f = 3.42 Hz (f) f = 8.34 Hz

Figure 2.6: Eigen mode shapes for L_{tot} = 80, α_l = 0.5, $\overline{E}$ = [10000, 10000]

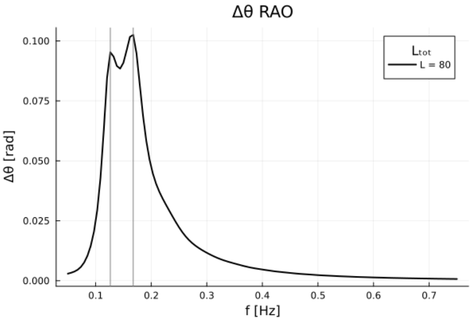

(a) RAO for L_{tot} = 80, α_l = 0.5, $\overline{E}$ = [10000, 10000]

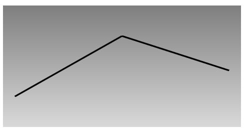

(b) Resonance shape f = 0.126

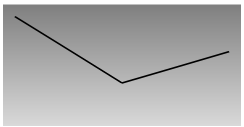

(c) Resonance shape f = 0.168

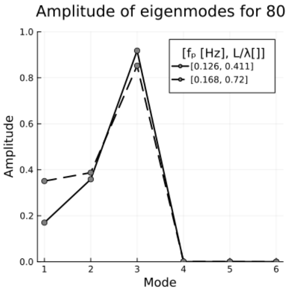

(d) Modal decomposition

Figure 2.7: Resonance shape decomposition

2.6. WEC optimisation and assessment

The WECs can be designed with a range of parameters. These parameters can be optimised in different manners to favour specific behaviour. This section will initiate with the parameters of interest and their respective ranges followed by the performance indicators. Subsequently, the method of optimisation is presented.

2.6.1. Parameters and performance indicators

This section presents the parameters and the performance indicators. First the parameters are shown, consequently the performance indicators are listed. This is followed by a motivation of each performance indicator. Finally the method to obtain the performance indicators is shown. To assess the wave energy converters, the influence of the following parameters is investigated:

- total length L_{tot}
- dimensionless PTO damping $\overline{c_r}$
- dimensionless raft stiffness $\overline{E}_{1,2}$
- aspect ratio of front raft α_l

The dimensionless PTO damping, raft stiffness, aspect ratio and draft are determined using equations (2.42), (2.43), (2.44) and (2.45)

$$\overline{c_r} = \frac{c_r\sqrt{gd}}{\rho g a L^4} \tag{2.42}$$

$$\overline{E} = \frac{E}{\rho g L} \tag{2.43}$$

$$\alpha_l = \frac{L_{b,1}}{L_{tot}} \tag{2.44}$$

$$\overline{d_0} = \frac{d}{L} \tag{2.45}$$

The range and stepsize of the parameters is determined using previous research [15, 16, 19, 17] and preliminary tests. This resulted in the ranges presented in equations (2.46), (2.47), (2.48), (2.49) and (2.50).

$$L_{tot} = [40,\ 60,\ 80,\ 100,\ 120,\ 140] \tag{2.46}$$

$$\alpha_l = [0.1,\ 0.2,\ 0.3,\ 0.4,\ 0.5] \tag{2.47}$$

$$\overline{E} = [[10;10],\ [100;100],\ [550;550],\ [1000;1000],\ [10000;10000]] \tag{2.48}$$

$$\overline{E} = [10,\ 100,\ 550,\ 1000,\ 10000] \tag{2.49}$$

$$\overline{E} = [10,\ 100,\ 10^{2.33},\ 10^{2.67},\ 1000,\ 10000] \tag{2.50}$$

To answer the research question the following key performance indicators have been chosen:

- The total annual energy conversion $\mathrm{E_{tot}}$
- The capture width CW
- The power spectrum

The total annual energy shows the sum of the annual energy conversion for all wave conditions. The annual energy conversion does not give insight into energy stability. Furthermore, it is prone to the distribution of the mean zero-crossing periods T_{av}, which vary per location. To gain more insight into the energy stability over the mean zero-crossing periods T_{av}, the capture width is plotted over the zero mean crossing periods. This allows for the assessment of energy stability, regardless of the total energy production. Both performance indicators are scaled by wave spectra dependent on zero-mean crossing periods. To assess the performance independent of wave conditions, the power spectrum is assessed.

The performance of the WEC is dictated by annual energy conversion and energy stability. In order to obtain these, the converted power spectrum needs to be determined. The power spectrum is computed by calculating the average power per frequency for a unit wave amplitude according to equation (2.51).

$$P_{ave} = \frac{1}{2} c_r \omega^2 \left(\Delta \frac{\partial \theta}{\partial t} \right)^2 \tag{2.51}$$

P_{ave} : Average converted power ω : angular frequency

Consequently, this power spectrum is scaled by the JONSWAP amplitude spectrum (2.28).

$$P_{sc}(f) = P_{ave}(f) S(f, T_p, H_s)^2 \tag{2.52}$$

P_{ave} : Scaled converted power

This results in the scaled power spectrum. To calculate the converted energy per half hour the scaled power spectrum is integrated over the frequencies, and multiplied by the time interval.

$$E_{30,j,k} = t_{30} \int_{f_{min}}^{f_{max}} P_{sc}(f) df \tag{2.53}$$

$E_{30,j,k}$: Half hourly converted energy for H_s[j] and T_p[k] $t_{30} = 1800$sec

The annual energy conversion for wave conditions (j,k) are obtained by multiplying the half hourly energy with the number of occurrences, see equation (2.54).

$$E_{\text{annual},j,k} = E_{30,j,k} n_{j,k} \tag{2.54}$$

$E_{\text{annual},j,k}$: Annual converted energy for H_s[j] and T_p[k] n : number of occurances

The total annual energy conversions results from the sum of the annual converted energy over all wave conditions.

$$E_{\text{tot}} = \sum_{H_s} \sum_{T_{av}} E_{\text{annual},j,k} \tag{2.55}$$

In addition to the annual energy conversion and the power spectrum, the capture width is a performance indicator. The capture width is a ratio of the converted energy by the available energy. Because the system is entirely linear, both the incident power (P_{in}) and the scaled converted power (P_{sc}) have the same dependence on the significant wave height (H_s^2), which is why it is neglected for the capture width formulation. The available energy is the integral of the incident power shown in equation (2.56).

$$P_{\text{in}} = \int \left(\rho_w g \frac{\omega}{2k} \left(1 + \frac{2kd}{\sinh(2kd)} \right) S(f) \right) df \tag{2.56}$$

This is used to calculate the capture width in equation (2.57)

$$CW(T_{av}) = \frac{\int P_{sc}(f)(T_{av}) df}{P_{in}(f)(T_{av})} \tag{2.57}$$

CW : Capture width

2.6.2. Parameter optimisation

There is a strong coupling between the design parameters, see figure 2.8. The figure shows that dependent on the PTO damping parameter ($\overline{c}$) each total length can appear optimal. Therefore, a combined analysis is required. To asses the different WEC configurations, the optimum damping parameter needs to be determined for each configuration, this procedure is summarised in figure 2.9. For each configuration a range of damping parameters is tested, resulting in the interpolated curve shown in figure 2.8. The maximum of this interpolation determines the optimum damping parameter. The accuracy of the interpolation is assessed in subsection 3.2.4. Once the optimum damping parameter is determined the experiment is run again to provide the true annual energy conversion, capture width and power spectrum for the optimum PTO damping parameter. Finally the performance indicators of the configurations with their respective optimum damping parameters are compared to each other.

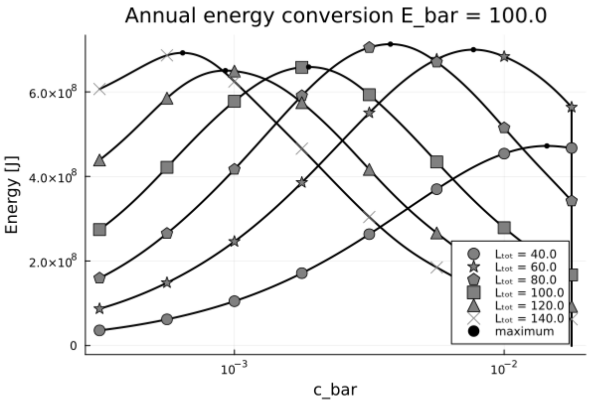

Figure 2.8: Annual energy production (E_{tot}) for various damping parameters ($\overline{c}$), and total lengths, for a symmetrical stiffness of $\overline{E} = [100, 100]$

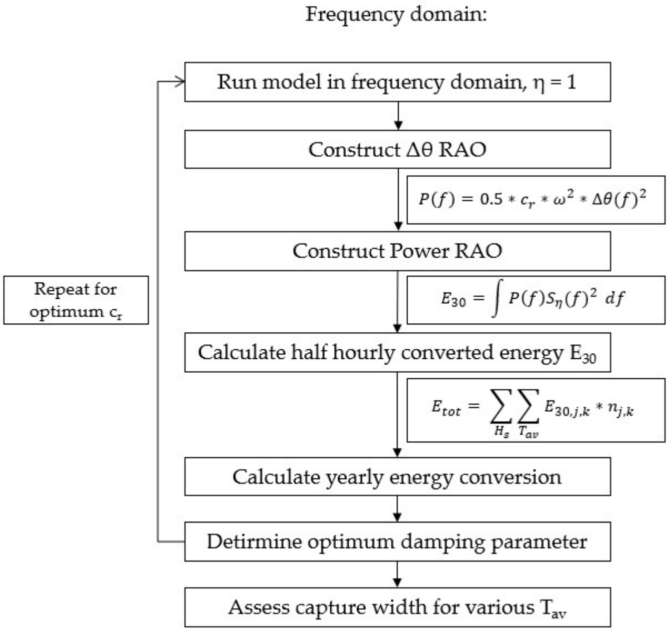

Figure 2.9: Optimisation plan

3

Numerical formulation

In order to asses the problem posed in the previous chapter a finite element model is constructed. This chapter describes the numerical formulation required for the FEM. Furthermore, it provides the verification and validation of the model. Figure 2.1 shows how the domain is distributed in separate sections.

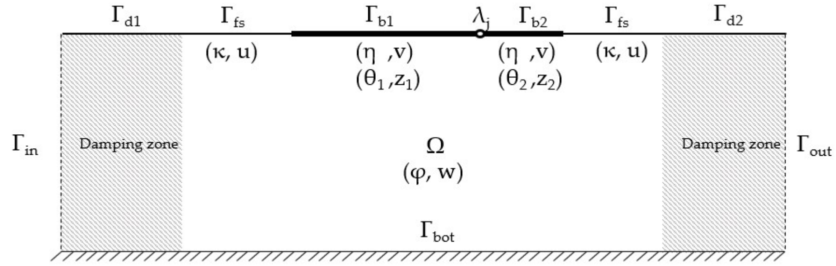

Figure 3.1: Overview of the domain, showing FEM symbols

Γ_{in} : Incident boundary domain
Γ_{d1} : Incident damping domain
Γ_{fs} : Free surface domain
Γ_{b1} : Fore raft domain
Γ_{b2} : Aft raft domain
Γ_{d2} : Outgoing damping domain
Γ_{out} : Outgoing boundary domain
Γ_{bot} : Bottom boundary domain
λ_j : Joint interface
Ω : Fluid domain
κ : Free surface elevation trail function
u : Free surface elevation test function
η : Structure elevation trail function
v : Structure elevation test function
θ_1 : Fore raft rotation trail function
z_1 : Fore raft rotation test function
θ_2 : Aft raft rotation trail function
z_2 : Aft raft rotation test function
ϕ : velocity potential trail function
w : Velocity potential test function

3.1. Weak form

The equations posed in chapter 2 are strong forms. The strong form is a differential equation, which has to be met at every point in the domain it describes. To solve the problem with a FEM, the continuity requirements need to be weakened to allow for a discretised solution. The weak form allows the condition to vary locally as long as the integral over the general domain is satisfied. The function can be weakened so that it is met in an average sense by using an integral expression that implicitly contains the strong form. This section will expand the weak form step by step. The first step is constructing the weak form for the fluid domain and separating the domain and the boundaries. Consequently, the boundary conditions for the free surface, structure interface, incident and outgoing boundary and bottom are expanded. Finally, the complete weak form is presented.

3.1.1. Derivation weak form, separation domain and boundaries

The derivation of the weak form is initiated by weakening the linear potential flow equation for the full domain. This is done by multiplying the continuous linear potential flow equation (3.1) by a test function and integrating it over the full domain, See equation (3.2).

$$\nabla^2\phi = 0 \tag{3.1}$$

$$\int \nabla^2\phi\cdot w\ d\Omega = 0 \tag{3.2}$$

Subsequently, the order of the differential can be reduced by applying integration by parts. Additionally, this allows for the boundary condition to be included, which results in the weak form presented in equation (3.3)

$$\int \nabla^2\phi\cdot w d\Omega = -\int_\Omega \nabla\phi\cdot\nabla w\ d\Omega + \int_\Gamma (\vec{n}\cdot\nabla\phi)\cdot w\ d\Gamma \tag{3.3}$$

In equation (3.3) Γ represents all boundaries, these will be separated in the next subsections. For simplicity let's define the following shorthand notation, where u represents the trial function, v the test function and $_\Omega$ the integral domain:

$$(u,\ v)_\Omega \simeq \int_\Omega u(x)v(x)d\Omega \qquad (u,\ v)_\Gamma \simeq \int_\Gamma u(x)v(x)d\Gamma$$

Furthermore, the time derivative will also be noted by a shorthand notation, presented below

$$\frac{\partial\kappa}{\partial t} = \kappa_t \qquad\qquad \frac{\partial^2\kappa}{\partial t^2} = \kappa_{tt}$$

The boundary Γ can be separated in the surface, structural, incident, outgoing and bottom boundary boundaries. The righthand side of equation (3.3) is equal to zero, separating it and taking it to the lefthand side results in equation (3.4)

$$(\nabla\phi,\ \nabla w)_\Omega - ((\vec{n}\cdot\nabla\phi),w)_{\Gamma_{\text{surface}}} - ((\vec{n}\cdot\nabla\phi),w)_{\Gamma_{\text{str}}} - ((\vec{n}\cdot\nabla\phi),w)_{\Gamma_{\text{in}}} - ((\vec{n}\cdot\nabla\phi),\ w)_{\Gamma_{\text{bottom}}} - ((\vec{n}\cdot\nabla\phi),\ w)_{\Gamma_{\text{out}}} = 0 \tag{3.4}$$

The next step is substituting the trail functions with the boundary conditions, this is done in the subsequent paragraphs.

3.1.2. Surface

The surface consists of the free surface and both damping zones. The boundary conditions for the free surface from section 2.3 are repeated in equations (3.5) and (3.6).

$$\text{Kinematic B.C.}: \qquad \frac{\partial\phi}{\partial z} = \kappa_t \tag{3.5}$$

$$\text{Dynamic B.C.}: \qquad 0 = \phi_t + g\kappa \tag{3.6}$$

The kinematic boundary is multiplied by the test function w. To guarantee the stability of the numerical system, coercivity must be guaranteed. O. Colomes et al. [30] have proven that numerical stability is guaranteed when the dynamic boundary condition is multiplied by the test function $\alpha_f w + u$ and weighted by β_h. This results in equation (3.7).

$$((\vec{n}\cdot\nabla\phi),w)_{\Gamma_{\text{fs}}} = (\kappa_t,\ u)_{\Gamma_{fs}} - \beta_h(\phi_t + g\kappa,\ \alpha_f w + u)_{\Gamma_{fs}} \tag{3.7}$$

Where α_f and β_h are given by equation (3.8) according to O. Colomes et al. [30].

$$\alpha_f = \frac{-i\omega}{\beta_h g}\left[1-\beta_h\right] \qquad\qquad \beta_h = 0.5 \tag{3.8}$$

The boundary conditions for the damping zones are repeated in equations (3.9), (3.10), (3.11) and (3.12).

$$\text{Incident kinematic B.C.}: \qquad \phi_t = -g_\kappa \tag{3.9}$$

$$\text{Incident dynamic B.C.}: \qquad \kappa_t = \frac{\partial\phi}{\partial z} - \mu_1(\kappa - \kappa_{in}) - \mu_2\left(\phi - \phi_{in}\right) \tag{3.10}$$

$$\text{Outgoing kinematic B.C.}: \qquad \phi_t = -g_\kappa \tag{3.11}$$

$$\text{Outgoing dynamic B.C.}: \qquad \kappa_t = \frac{\partial\phi}{\partial z} - \mu_1\kappa - \mu_2\phi \tag{3.12}$$

Similar to the free surface, the kinematic boundary condition of the damping zone is multiplied with the test function w, whereas the dynamic boundary condition is multiplied with the test function $\alpha_f w + u$ and weighted by β_h for coercivity. This results in equations (3.13) and (3.14).

$$((\vec{n}\cdot\nabla\phi), w)_{\Gamma_{d1}} = (\kappa_t,\ u)_{\Gamma_{d1}} - \beta_h(\phi_t + g\kappa,\ \alpha_f w + u)_{\Gamma_{d1}} + (\kappa_t + \mu_{1,in}\kappa - \frac{\mu_{2,in}}{g\phi}, w)_{\Gamma_{d1}} \tag{3.13}$$

$$((\vec{n}\cdot\nabla\phi), w)_{\Gamma_{d2}} = (\kappa_t,\ u)_{\Gamma_{d2}} - \beta_h(\phi_t + g\kappa,\ \alpha_f w + u)_{\Gamma_{d2}} + (\kappa_t + \mu_{1,out}\kappa - \frac{\mu_{2,out}}{g\phi}, w)_{\Gamma_{d2}} \tag{3.14}$$

3.1.3. Structure

The structure boundary consists of the fore raft, the aft raft and the jointed connection. The equations of motion of the structure from section 2.2 are repeated in equations (3.15) and (3.16).

$$\rho A\eta_{tt} = kGA\left(\frac{d\eta^2}{dx^2} - \frac{d\theta}{dx}\right) + p \tag{3.15}$$

$$\rho I\theta_{tt} = EI\frac{d\theta^2}{dx^2} + kGA\left(\frac{d\eta}{dx} - \theta\right) \tag{3.16}$$

The structural equations of motion are coupled to the fluid by the pressure term p in the dynamic boundary condition in equation (3.17).

$$\frac{p}{\rho_w} = -\frac{\partial\phi}{\partial t} - g\eta \tag{3.17}$$

Furthermore the kinematic boundary condition for the structure elevation results in equation (3.18).

$$\text{Kinematic B.C.}: \frac{\partial\phi}{\partial z} \qquad = \eta_t \tag{3.18}$$

The dynamic boundary condition is substituted in equations (3.15), (3.16). Dividing everything by ρ_w results in the draft term (d_0), subsequently rewriting the time derivative with subscript notation results in equations (3.19), (3.20).

$$d_0\eta_{tt} + \phi_t + g\eta = kGA\nabla\left(\nabla\eta - \theta\right) \tag{3.19}$$

$$\rho I\theta_{tt} = EI\nabla^2\theta + kGA\left(\nabla\eta - \theta\right) \tag{3.20}$$

d_0 : Draft

Subsequently, the weak form is constructed by multiplying the test function with the trial functions and integrating, see equations (3.21) and (3.22):

$$(d_0\eta_{tt} + \phi_t + g\eta,\ v)_{\Gamma_{b1}} - (kGA\nabla\left(\nabla\eta - \theta\right),\ v)_{\Gamma_{b1}} = 0 \tag{3.21}$$

$$(\rho I\theta_{tt},\ z_1)_{\Gamma_{b1}} - (EI\nabla^2\theta + kGA\left(\nabla\eta - \theta\right),\ z_1)_{\Gamma_{b1}} = 0 \tag{3.22}$$

Next, integration by parts is applied, to reduce the order and allow for the substitution of the boundary conditions, resulting in equations (3.23) and (3.24).

$$\begin{aligned}(d_0\eta_{tt}+\phi_t+g\eta,\ v)_{\Gamma_{b1}}+(kGA\big(\nabla\eta-\theta\big),\ \nabla v)_{\Gamma_{b1}}-(\vec{n}\ kGA\big(\nabla\eta-\theta\big),\ v)_{\Lambda_{b1}}&=0 \qquad (3.23)\\ (\rho I\theta_{tt},\ z_1)_{\Gamma_{b1}}-(kGA\big(\nabla\eta-\theta\big),\ z_1)_{\Gamma_{b1}}+(EI\nabla\theta,\ \nabla z_1)_{\Gamma_{b1}}-(\vec{n}\ EI\nabla\theta,\ z_1)_{\Lambda_{b1}}&=0 \qquad (3.24)\end{aligned}$$

Here Λ_{b1} represents the boundaries of the beam. This can be separated in the free end and the joint, see equations (3.25) and (3.26).

$$\begin{aligned}(\vec{n}\ kGA\big(\nabla\eta-\theta\big),\ v)_{\Lambda_{b1}}&=(\vec{n}\ kGA\big(\nabla\eta-\theta\big),\ v)_{\Lambda_{free}}+(\vec{n}\ kGA\big(\nabla\eta-\theta\big),\ v)_{\Lambda_j} \qquad (3.25)\\ (\vec{n}\ EI\nabla\theta,\ z_1)_{\Lambda_{b1}}&=(\vec{n}\ EI\nabla\theta,\ z_1)_{\Lambda_{free}}+(\vec{n}\ EI\nabla\theta,\ z_1)_{\Lambda_j} \qquad (3.26)\end{aligned}$$

$$\Lambda_{free}:\text{Free boundary beam}$$

The interface conditions from section 2.2 are repeated in equations(3.27), (3.28), (3.29) and (3.30).

$$\begin{aligned}\text{constant displacement}:&\qquad \eta_1^+=\eta_2^- && (3.27)\\ \text{constant shear}:&\qquad kGA\left(\frac{\partial\eta_1}{\partial x}-\theta_1\right)=kGA\left(\frac{\partial\eta_2}{\partial x}-\theta_2\right) && (3.28)\\ \text{Constant moment}:&\qquad EI_1\frac{\partial\theta_1}{\partial x}\ =\ EI_2\frac{\partial\theta_2}{\partial x}\ =\ M_c && (3.29)\\ \text{Damping moment}:&\qquad M_c=c_r\left(\theta_{1,t}-\theta_{2,t}\right) && (3.30)\end{aligned}$$

At the free boundary of the structure the shear and moment are equal to zero. At the joint end, the interface conditions posed in equations (3.27), (3.28), (3.29) and (3.30) need to be satisfied. By applying the same test function η over both structures the constant shear and displacement criteria, equations 3.28 and (3.27), are satisfied. Finally, the constant moment is set equal to the damping moment. This results in equation (3.31)

$$\begin{aligned}((\vec{n}\cdot\nabla\phi),w)_{\Gamma_{\text{str}}}=&(d_0\eta_{tt}+g\eta-\phi_t,\ v)_{\Gamma_{b1}}+(I\theta_{1,tt}+\alpha_{1,1}\nabla\theta_1,\ z_1)_{\Gamma_{b1}}-(\alpha_{2,1}(\nabla\eta-\theta_1),\ \nabla v-z_1)_{\Gamma_{b1}}\\ &(d_0\eta_{tt}+g\eta-\phi_t,\ v)_{\Gamma_{b2}}+(I\theta_{2,tt}+\alpha_{1,2}\nabla\theta_2,\ z_2)_{\Gamma_{b2}}-(\alpha_{2,2}(\nabla\eta-\theta_2),\ \nabla v-z_2)_{\Gamma_{b2}}\\ &+(c_r/\rho_w(\theta_{1,t}^+-\theta_{2,t}^-),\ (z_1^+-z_2^-))_{\Lambda_j}\end{aligned} \qquad (3.31)$$

$$\alpha_{1,i}=\frac{EI_i}{\rho_w} \qquad\qquad \alpha_{2,i}=\frac{kGA}{\rho_w} \qquad (3.32)$$

To complete the formulation of the structure interface, the kinematic boundary condition, equation (3.18), results in the final two terms in equation (3.33)

$$\begin{aligned}((\vec{n}\cdot\nabla\phi),w)_{\Gamma_{\text{str}}}=&(d_0\eta_{tt}+g\eta-\phi_t,\ v)_{\Gamma_{b1}}+(I\theta_{1,tt}+\alpha_1\nabla\theta_1,\ z_1)_{\Gamma_{b1}}-(\alpha_2(\nabla\eta-\theta_1),\ \nabla v-z_1)_{\Gamma_{b1}}\\ &(d_0\eta_{tt}+g\eta-\phi_t,\ v)_{\Gamma_{b2}}+(I\theta_{2,tt}+\alpha_1\nabla\theta_2,\ z_2)_{\Gamma_{b2}}-(\alpha_2(\nabla\eta-\theta_2),\ \nabla v-z_2)_{\Gamma_{b2}}\\ &+(c_r/\rho_{ww}(\theta_{1,t}^+-\theta_{2,t}^-),\ (z_1^+-z_2^-))_{\Lambda_j}+(\eta_t,\ w)_{\Gamma_{b1}}+(\eta_t,\ w)_{\Gamma_{b2}}\end{aligned} \qquad (3.33)$$

3.1.4. Incident boundary

Section 2.3 showed that for the incident boundary, the normal velocity needs to be equal to the wave velocity, this is repeated in equation (3.34):

$$v_{x,in}=\frac{\partial\phi}{\partial x} \qquad (3.34)$$

Implementing this in the weak form results in equation (3.35).

$$((\vec{n}\cdot\nabla\phi),w)_{\Gamma_{\text{in}}}=(v_{\text{x,in}},w)_{\Gamma_{\text{in}}} \qquad (3.35)$$

3.1.5. Outgoing boundary

Section 2.3 showed that the normal velocity is equal to zero at the outgoing boundary, as is shown in equation (3.36).

$$\frac{\partial \phi}{\partial x} = 0 \tag{3.36}$$

This results in equation (3.37)

$$(\vec{n} \cdot \nabla \phi), w)_{\Gamma_{\text{in}}} = 0 \tag{3.37}$$

3.1.6. Bottom boundary

Section 2.3 showed that the normal velocity is equal to 0 at the bottom boundary, see equation (3.38).

$$\frac{\partial \phi}{\partial z} = 0 \tag{3.38}$$

This results in equation (3.39).

$$(\vec{n} \cdot \nabla \phi), w)_{\Gamma_{\text{bot}}} = 0 \tag{3.39}$$

3.1.7. Complete weak form

The previous sections showed the derivation of the weak form for the fluid domain, structural domain and all the boundary terms. Implementing equations (3.7), (3.33), (3.35), (3.37) and (3.39) in equation (3.4), and taking the known terms to the righthand side results in the complete weak form, see equation (3.40).

$$\begin{aligned}
(\nabla \phi,\ \nabla w)_{\Omega} - \\
(\kappa_t,\ u)_{\Gamma_{fs}} + \beta_h(\phi_t + g\kappa,\ \alpha_f w + u)_{\Gamma_{fs}} + \\
(\kappa_t,\ u)_{\Gamma_{d1}} + \beta_h(\phi_t + g\kappa + \phi_t,\ \alpha_f w + u)_{\Gamma_{d1}} - (\kappa_t + \mu_{1,in}\kappa - \mu_{2,in}/g\phi, w)_{\Gamma_{d1}} + \\
(\kappa_t,\ u)_{\Gamma_{d2}} + \beta_h(\phi_t + g\kappa + \phi_t,\ \alpha_f w + u)_{\Gamma_{d2}} - (\kappa_t + \mu_{1,out}\kappa - \mu_{2,out}/g\phi, w)_{\Gamma_{d2}} + \\
(d_0\eta_{tt},\ v)_{\Gamma_{b1}} + (g\eta - \phi_t,\ v)_{\Gamma_{b1}} + (I\theta_{1,tt} + \alpha_1\nabla\theta_1,\ z_1)_{\Gamma_{b1}} - (\alpha_2(\nabla\eta - \theta_1),\ \nabla v - z_1)_{\Gamma_{b1}} + (\eta_t,\ w)_{\Gamma_{b1}} + \\
(d_0\eta_{tt},\ v)_{\Gamma_{b2}} + (g\eta - \phi_t,\ v)_{\Gamma_{b2}} + (I\theta_{2,tt} + \alpha_1\nabla\theta_2,\ z_2)_{\Gamma_{b2}} - (\alpha_2(\nabla\eta - \theta_2),\ \nabla v - z_2)_{\Gamma_{b2}} + (\eta_t,\ w)_{\Gamma_{b2}} + \\
(c_r/\rho_w(\theta^+_{1,t} - \theta^-_{2,t}),\ (z^+_1 - z^-_2))_{\Lambda_j} \\
= (v_{\text{x,in}}, w)_{\Gamma_{\text{in}}} + (\eta_d + \phi_d/g, w)_{\Gamma_{d1}}
\end{aligned} \tag{3.40}$$

η_d : Surface elevation with damping terms

ϕ_d : Velocity potential with damping terms

3.2. Validation and verification

Before the results of a numerical model are deemed trustworthy, the model needs to be verified and validated. Verification means checking that the model shows behaviour which is in line with its theoretical basis. In this case, this entails a convergence check of the L2-norm of the error and the energy conservation. Validation checks the accuracy of a model's representation of a real system. This model is validated by comparing the results of previous numerical works to the model's results.

3.2.1. Mesh size

The mesh size refers to the size of the mesh used to discretize the domains. To assess the influence of the mesh size the L2 norm of the error is computed. The error is computed for velocity potential (ϕ) and the surface elevation (η, κ) of the model without structure. This allows comparing the model results with the analytical wave formulation and verifies the modelling of the water and the damping zone. The error is computed according to equations(3.41), (3.42) and (3.43).

$$e_\phi = \phi_{in} - \phi_h \tag{3.41}$$

$$e_\eta = \eta_{in} - \eta_h \tag{3.42}$$

$$e_\kappa = \kappa_{in} - \kappa_h \tag{3.43}$$

ϕ_h : Result velocity potential η_h : Result structure elevation κ_h : Result surface elevation

Consequently, the error is used to compute the error norm in equations (3.44) and (3.45).

$$L2_\phi = \sqrt{\sum \int |e_\phi^2| \, d\Omega_t} \tag{3.44}$$

$$L2_{\eta,\kappa} = \sqrt{\sum \int |e_\eta^2| \, d\Gamma_t} + \sqrt{\sum \int |e_\kappa^2| \, d\Gamma_t} \tag{3.45}$$

The number of elements in the x-direction is governed by the number of elements n_x in the fore raft. This number is then extrapolated the determine the total number of elements in the x-direction. Furthermore, the mesh spacing in the y-direction is exponential such that the surface has a higher resolution than the bottom. This is done because wave motion decreases logarithmically to the sea-bed. Figure 3.2 shows the convergence for regular harmonic waves in the time domain for parameters in table 3.1. All orders converge with a convergence rate of order +1 to a level at which the error norm stagnates. This stagnation is due to the influence of the damping zones which transmit a small error into the domain.

Table 3.1: Physical and numerical parameters for mesh convergence test

Domain dimensions	:	L_{fs}	= 40 m	L_d	= 30 m	d	= 1.1 m
Numerical parameters	:	Δt	= 0.005 s	t_f	= 2Δ t	n_y	= 32
Wave properties	:	κ_0	= 0.01 m	λ	= 0.42 m		

L_{fs} : Free surface length L_d : Damping zone length Δt : Time interval
t_f : End time test n_x : Number of elements in x, in fore raft n_y : Number of elements in y
λ : Wave length O : Polynomial order test function

3.2.2. Energy conservation

In order to assess the functioning of the damping zones the system has to be energy-conserving, meaning that there is no energy accumulation over time. To assess this, the potential and kinetic energy in the true domain (e.g. excluding the damping zone), are compared to the energy resulting from the incident wave profile, using the parameters in table 3.2, see equations (3.47) and (3.46).

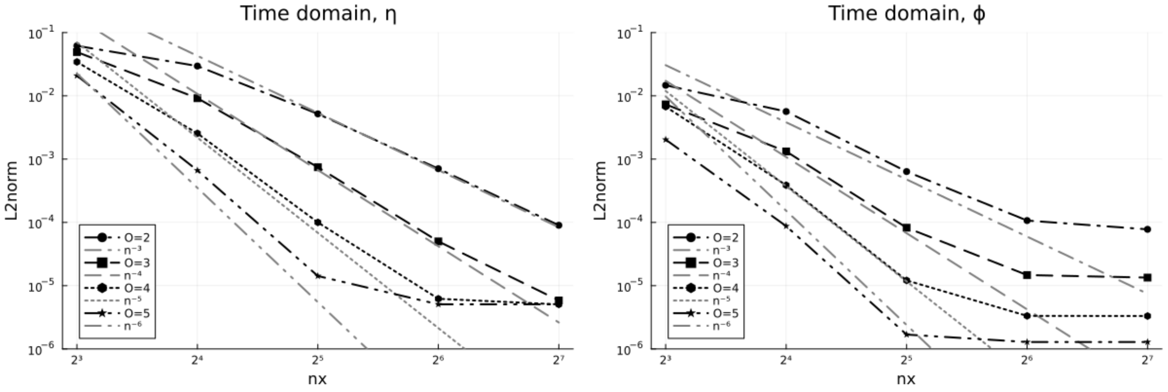

(a) Surface elevation η

(b) Velocity potential ϕ

Figure 3.2: L2-norm of the error for surface elevation and velocity potential

$$E_K = \frac{\rho_w}{2}\iint_{\Omega_t} \nabla\phi^2 \, d\Omega \tag{3.46}$$

$$E_P = \frac{\rho_w g}{2}\iint_{\Gamma_t} \eta^2 \, d\Gamma \tag{3.47}$$

E_K : Kinetic energy E_P : Potential energy Ω_t : True domain Γ_t : True boundaries

Figure 3.3 shows the energy in the system for a regular wave. The figure shows that after an initial start phase, the energy level does not accumulate, and does not exceed the energy introduced into the system by the incident waves. This proves that no reflection occurs at the boundaries. Thus, the damping zones function accordingly and the model is stable.

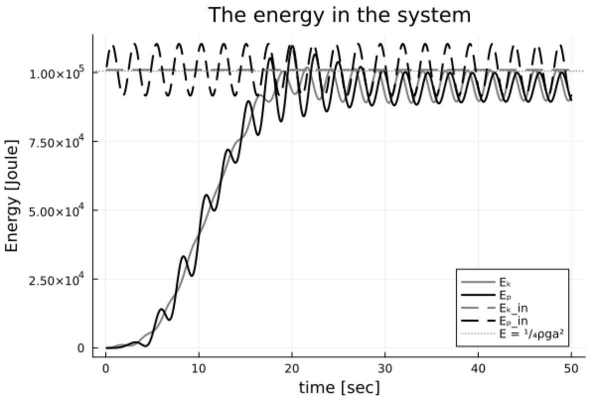

Figure 3.3: Energy in the domain for a regular wave

3.2.3. Model validation

In order to validate the present model, the model is compared with the models of Colomes et al. [30] and Khabekhpasheva et al. [31]. Both researches constructed a model for monochromatic waves with a floating

Table 3.2: Physical and numerical parameters for energy conservation test

Domain dimensions	:	L_{fs}	= 40 m	L_d	= 30 m	d	= 50 m				
Numerical parameters	:	Δt	= 0.005 s	t_f	= 2Δ t	n_x	= 64	n_y	= 6	O	= 3
Wave properties	:	κ_0	= 1.00 m	Λ	= 36 m						

Euler Bernoulli beam, solved in the frequency. In order to compare the results the parameters shown in table 3.3 are used. Furthermore, the shear modulus and cross-sectional area are estimated by using the slenderness ratio (2.3), where the slenderness ratio is set to 10.000 to minimise the error between Timoshenko and Euler Bernoulli approximation. Figure 3.4 shows the normalised deflection for structure with and without joint in figures 3.4a and 3.4b respectively. The figure shows that the results are in agreement with those of Colomes et al. [30] and Khabekhpasheva et al. [31].

Table 3.3: Physical and numerical parameters used for validation according to Colomes et al. [30] and Khabekhpasheva et al. [31]

Domain dimensions	:	L_{fs}	= 6.25 m	L_{tot}	= 12.5 m	L_d	= 12.5 m	d	= 1.1 m
Structural properties	:	EI_1	= 47100 m^2	EI_2	= 471 m^2	α_l	= 0.2	d_0	= 8.2 mm
Numerical parameters	:	n_x	= 2	n_y	= 5	O	= 4		
Wave properties	:	κ_0	= 0.01 m	Λ	= 3.11 m				

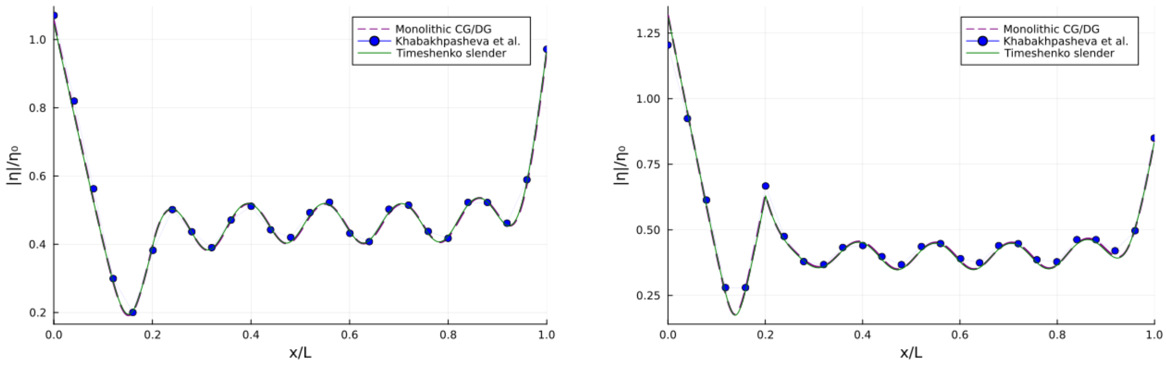

(a) Structure without joint

(b) Structure with joint

Figure 3.4: Model validation of a floating structure, compared to the research [30], [31]

3.2.4. Interpolation validation

This section compares the interpolated annual energy conversion to the results from the model. The optimum damping parameter is selected by calculating the annual energy conversion, and interpolating these results to find the maximum, see section 2.6.2. The error between the interpolated annual energy conversion and the computed annual energy conversion is presented in table 3.4. The table shows that the average error is 0.5%. Therefore, it can be concluded that the interpolation gives a good prediction of the annual energy conversion, and hence the optimum damping parameter. In addition to this, interpolation is only used to determine the optimum damping parameters. The final results are obtained by repeating the test with the optimum damping parameter.

Table 3.4: Interpolation error of annual energy

L_{tot} [m]	40	60	80	100	120	140
Interpolated E_{tot} [J]	4.722e8	6.999e8	7.130e8	6.589e8	6.504e8	6.923e8
Result E_{tot} [J]	4.728e8	6.988e8	7.118e8	6.584e8	6.484e8	6.851e8
Error	0.9%	0.2%	0.2%	0.1%	0.3%	1.1%

4

Results and Discussion

This chapter contains the results from the numerical experiments. The chapter is initiated by an eigenmode analysis for the undamped system. This section clarifies the influence of individual parameters by identifying the eigenfrequencies and eigenmode shapes. Consequently, the resonance shapes of the hydraulically damped system from the RAO are decomposed by the eigenmodes according to the method described in section 2.5.3. The decomposition shows the contribution of modes in the resonance shape, thereby it relates the response of the hydraulically damped system to the modal analysis. The second half of the chapter reports the results from the WEC optimisation for the combined effects of total length, aspect ratio, raft stiffness and PTO damping. This section investigates the combined effects on annual energy conversion and energy stability.

4.1. Eigen modes and frequencies of undampened structures

This section reports the eigenmode analysis for the undamped system and decomposes the real resonance shapes of the $\Delta\theta$ RAO for various hydraulically damped systems according to section 2.5.3. The eigenmode and frequency analysis is divided into four subsections. The first two subsections contain the eigenmodes and frequencies for symmetrical structures, i.e. an aspect ratio of $\alpha_L = 0.5$ and the same stiffness for fore and aft raft $\overline{E}_1 = \overline{E}_2$. The two following subsections report the eigenmode shapes and frequencies of asymmetric structures i.e. $\alpha_l \neq 0.5$ or $\overline{E}_1 \neq \overline{E}_2$. Each subsection investigates the influence of that parameter, while the other parameters remain equal to the values shown in table 4.1.

Table 4.1: Standard parameters for eigenmode testing

L_{tot}	$\overline{E_1}$	$\overline{E_2}$	α_l	$\overline{c}$	$\overline{d_0}$
80	10000	10000	0.5	0	0.005

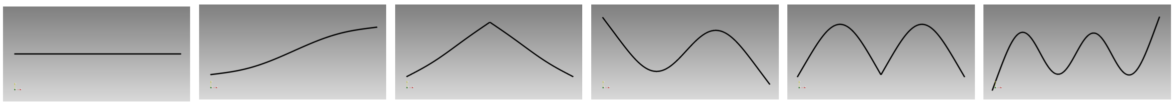

(a) 1^{st} mode (b) 2^{nd} mode (c) 3^{rd} mode (d) 4^{th} mode (e) 5^{th} mode (f) 6^{th} mode

Figure 4.1: Eigen mode shapes of symmetric structures, corresponding frequencies are shown in figure 4.2a and 4.4a

4.1.1. Total length

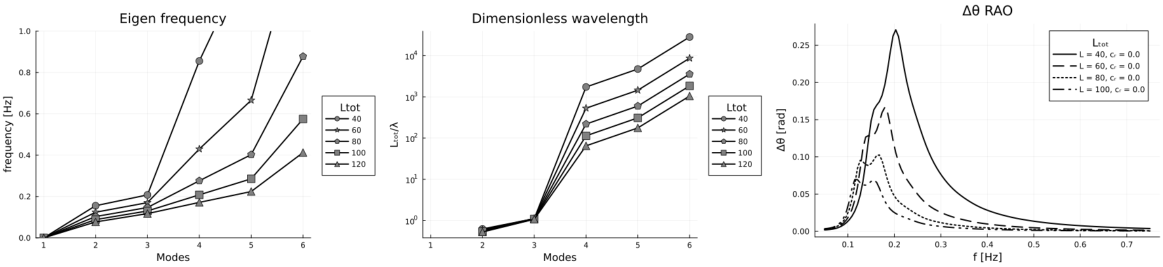

(a) Eigen frequencies for various L_{tot}

(b) $\frac{L}{\lambda} \equiv f_n$ for various L_{tot}

(c) $\Delta\theta$ RAO for various L_{tot}

Figure 4.2: Eigen frequencies, dimensionless wavelength and $\Delta\theta$ RAO for various L_{tot} and constant $\overline{E}$ = [10000; 10000], $\alpha_l = 0.5$, $\overline{c} = 0$, $\overline{d_0} = 0.005$

The total length refers to the length of both rafts combined. The first six eigenmodes are shown in figure 4.1. The influence of the total WEC length on the first six eigenfrequencies is shown in figure 4.2a. The figure shows that the first mode is unaffected, whereas all other eigenfrequencies are influenced by the length. Furthermore, it shows that increasing L_{tot} decreases the eigenfrequencies.

The frequencies in figure 4.2a can be converted into hydraulic wavelengths using the dispersion relation. Subsequently, this wavelength can be made dimensionless by dividing it by the total WEC length. This results in the modal dimensionless wavelengths shown in figure 4.2b. The first mode is pure heave and has a frequency of $f \approx 0$ and is therefore omitted. Figure 4.2b shows that the dimensionless wavelength for the second and third modes are hardly affected by the total length. For completely rigid structures a dimensionless wavelength of $\frac{L_{tot}}{\lambda} = \frac{1}{2} \vee 1$ is expected for the second and third modes. Table 4.2 shows the dimensionless wavelengths for the second and third eigenmode, resultant from the model. The second mode has a dimensionless wavelength of $\frac{L}{\lambda} \approx 0.58$. The third mode has a dimensionless wavelength of $\frac{L}{\lambda} \approx 1.1$. This indicates that the first two modes are governed by rigid body motions. Both modes are overestimating the theoretical value. This is due to the neglect of the frequency-dependent added mass in the eigenmode analysis. In the decoupled system $\hat{\boldsymbol{K}}_{\boldsymbol{w\phi}}$ represents the hydraulic stiffness and frequency-dependent added mass, see equation (4.1).

$$\hat{\boldsymbol{K}}_{\boldsymbol{w\phi}} = \boldsymbol{K}_{\boldsymbol{w\phi}} + \omega^2 \boldsymbol{C}_{\boldsymbol{w\kappa}} \boldsymbol{K}_{\boldsymbol{u\kappa}}^{-1} \boldsymbol{C}_{\boldsymbol{u\phi}} \tag{4.1}$$

However the added mass term represented by the damping terms ($\boldsymbol{C}_{\boldsymbol{w\kappa}}, \boldsymbol{C}_{\boldsymbol{u\phi}}$), and the stiffness term ($\boldsymbol{K}_{\boldsymbol{u\kappa}}^{-1}$) has been neglected in the eigenvalue analysis, see section 2.5.2.

Table 4.2: Relation dimensionless wavelength and L_{tot}

L_{tot}	40	60	80	100
2^{nd} [L_{tot}/λ]	0.624	0.594	0.560	0.540
3^{rd} [L_{tot}/λ]	1.11	1.11	1.10	1.09

Figure 4.2b shows that for the fourth and higher mode, the dimensionless wavelength is influenced by the total length. This is due to the definition of the dimensionless stiffness coefficient $\overline{E}$, and the eigenfrequencies of a beam. The dimensionless stiffness is proportional to the ratio of Young's modulus over the length, whereas the eigenfrequencies of a beam are proportional to the square root of young's modulus over the fourth power of the length, see equation (4.2).

$$\overline{E} = \frac{E}{\rho_w g L} \qquad \omega_n \propto \sqrt{\frac{EI}{\rho_b A L^4}} \tag{4.2}$$

The difference in linear and squared proportionality results in a separation of dimensionless wavelengths for various total lengths.

Figure 4.2c shows the $\Delta\theta$ RAO of the system including hydraulic damping terms. The $\Delta\theta$ RAO shows two phenomena. Firstly, it shows a decrease of the peak frequency for increasing total WEC length, which is in line with the eigenfrequency analysis. Secondly, it shows that a smaller total length leads to a larger relative rotation $\Delta\theta$. This is in line with the goniometric relation shown in equation (4.3).

$$\theta_i = \arctan\left(\frac{\text{amplitude}}{\text{raft length}}\right) \tag{4.3}$$

The resonance shapes corresponding to the RAO peaks of 4.2c can be decomposed by modal analysis, see 2.5.3. Figure 4.3 shows the amplitudes of the modes, per resonance shape. Figure 4.3 shows that, because the eigenfrequencies decrease as the WEC length increases the eigenfrequencies come closer together, resulting in a more equal spread of modal amplitudes.

From these results the following conclusions are derived:

- Modes 2 and higher are affected by the total length.
- Eigen frequencies decrease for increasing total WEC lengths
- The dimensionless wavelength for the second and third modes can be approximated by $\frac{L}{\lambda} \approx 0.58 \vee 1.1$ respectively.
- There is a more equal spread of modal amplitudes as the total WEC length increases, indicating that the resonance shapes are less dependent on one mode.

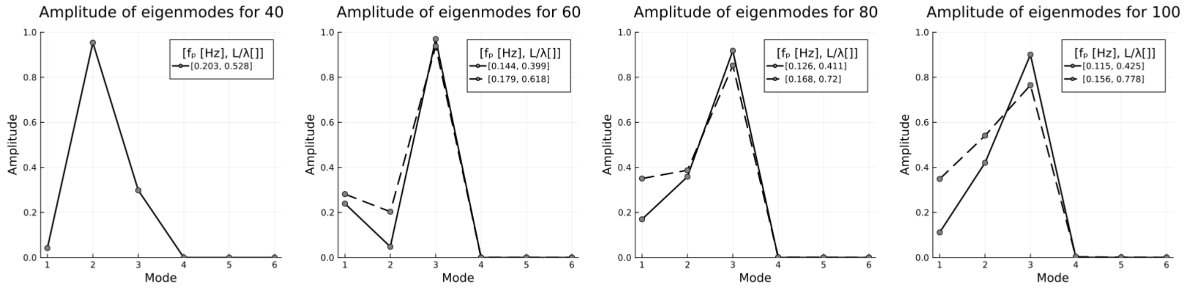

(a) $L_{tot} = 40$ (b) $L_{tot} = 60$ (c) $L_{tot} = 80$ (d) $L_{tot} = 100$

Figure 4.3: The modal decomposition of resonance shapes, corresponding to peak frequencies f_p and dimensionless wavelengths $\frac{L_{tot}}{\lambda}$, for variable L_{tot} and constant $\overline{E}$ = [10000; 10000], $\alpha_l = 0.5$, $\overline{c} = 0$, $\overline{d_0} = 0.005$

4.1.2. Symmetric raft stiffness

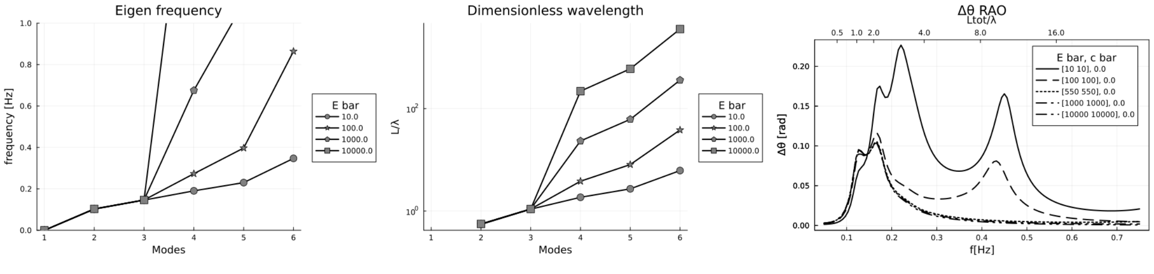

(a) Eigen frequencies for various symmetric $\overline{E}$ (b) $\frac{L}{\lambda} \equiv f_n$ for various symmetric $\overline{E}$ (c) $\Delta\theta$ RAO for various symmetric $\overline{E}$

Figure 4.4: variable symmetric $\overline{E}$ and constant L_{tot} = 80m, $\alpha_l = 0.5$, $\overline{c} = 0$, $\overline{d_0} = 0.005$

The symmetric raft stiffness refers to the same dimensionless raft stiffness for the fore and aft raft. The influence of the stiffness on the eigenfrequency, the dimensionless wavelength and $\Delta\theta$ RAO is shown in figure 4.4. Figure 4.4a shows that the first three eigenfrequencies are unaffected by the symmetric stiffness. Furthermore, it shows that the eigenfrequencies of mode four and above increase for increasing stiffness. Equation

(4.2) confirms this because elastic modes are proportional to the square root of the stiffness. This confirms that the first three modes are governed by rigid body motion and mode four and above by flexible behaviour. These results are reflected in the dimensionless wavelength, presented in figure 4.4b.

To analyse the RAO peaks, the resonance shapes corresponding to the peaks have been decomposed into eigenmodes according to the method described in section 2.5.3. Figure 4.4c shows $\Delta\theta$ RAO for four dimensionless stiffness coefficients. The increase of relative rotation $\Delta\theta$ at $f \approx 0.13$ combined with the increase of the modal amplitude of the third mode shows that the relative rotation due to rigid body motion increases for more stiff structures. Conversely, the increase of relative rotation $\Delta\theta$ for $f \geq 0.17$ combined with the increase of modal amplitudes of mode 4 and above, show that the relative rotation $\Delta\theta$ due to flexible behaviour increases for less stiff structures. Furthermore, figure 4.5 shows that because the eigenfrequencies of mode 4 and above increase for increasing raft stiffness, the amplitudes of these modes decrease for increasing raft stiffness.
From these results the following conclusions are derived:

- The first three modes are governed by rigid behaviour because the eigenfrequencies are not influenced by the symmetric stiffness.
- Modes 4 and above are governed by flexible behaviour because the eigenfrequencies are influenced by the symmetric raft stiffness.
- There are more modes present per resonance shape as the stiffness decreases because the eigenfrequencies move closer together, indicating that resonance shapes are less dependent on one mode.
- The relative rotation $\Delta\theta$ increases for rigid behaviour-governed modes and the $\Delta\theta$ decreases for flexible behaviour-governed modes as the raft stiffness increases, the inverse is true for flexible structures.

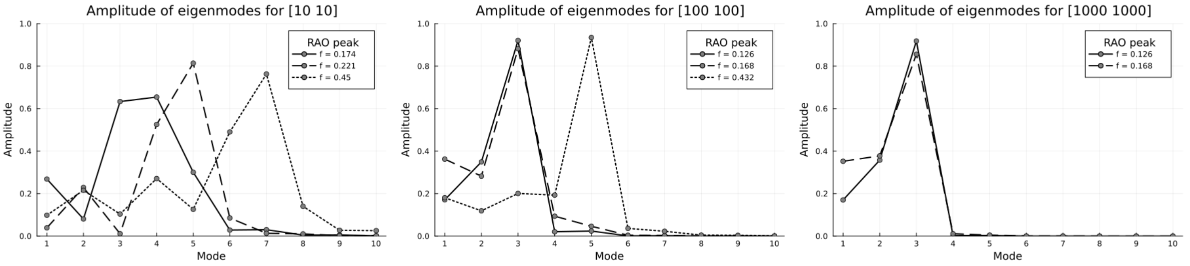

(a) $\overline{E} = [10, 10]$ (b) $\overline{E} = [100, 100]$ (c) $\overline{E} = [1000, 1000]$

Figure 4.5: The modal decomposition of various resonance shapes, corresponding to peak frequencies f_p and dimensionless wavelengths $\frac{L_tot}{\lambda}$, for variable symmetric $\overline{E}$ and constant $L_{tot} = 80$m, $\alpha_l = 0.5$, $\overline{c} = 0$, $\overline{d_0} = 0.005$

4.1.3. Aspect ratio

For asymmetric structures, the eigenfrequency and the eigenshape per mode change for changing parameters. figure 4.6 shows the eigenshapes for various aspect ratios α_l.

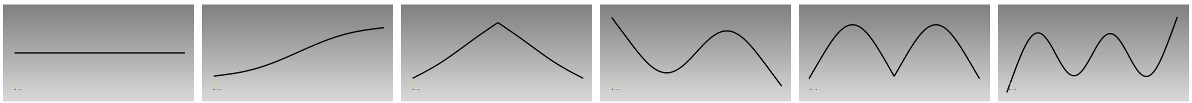

(a) $\alpha_l = 0.5$

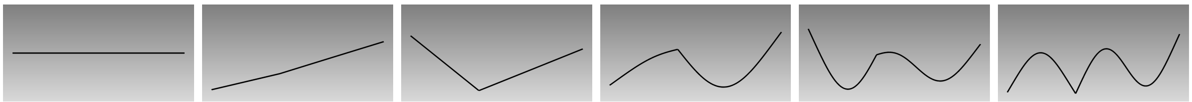

(b) $\alpha_l = 0.4$

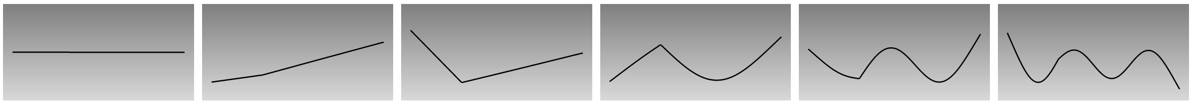

(c) $\alpha_l = 0.3$

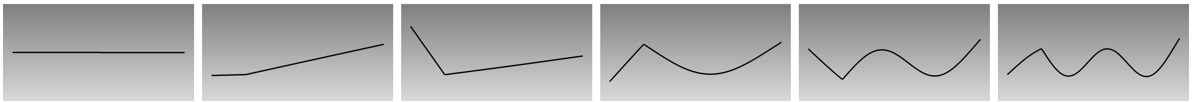

(d) $\alpha_l = 0.2$

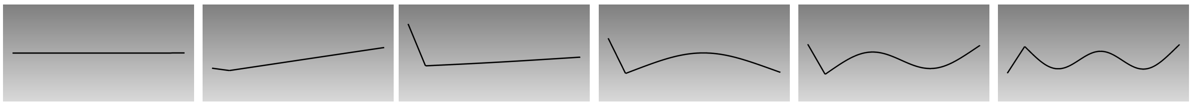

(e) $\alpha_l = 0.1$

Figure 4.6: The first six eigenshapes for various length ratios of the first raft, corresponding eigenfrequencies and dimensionless wavelengths are shown in figure 4.8, all multiplied by an amplification factor of 100, $L_{tot} = 80$, $\overline{E} = [10000, 10000]$, $\overline{d_0} = 0.005$

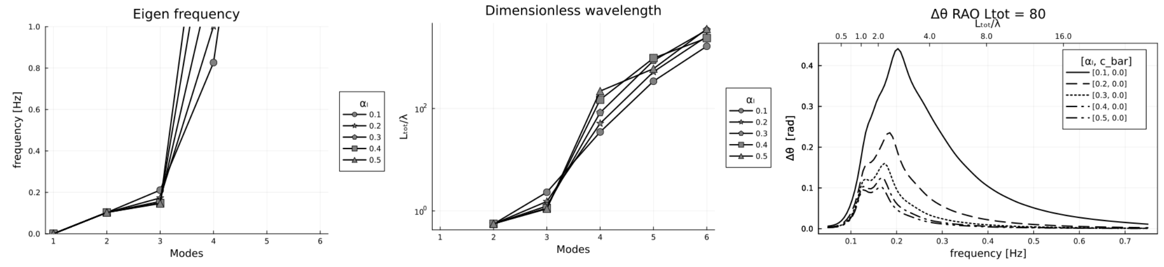

(a) Eigen frequencies for various α_l

(b) $\frac{L}{\lambda} \equiv f_n$ for various α_l

(c) $\Delta\theta$ RAO for various α_l

Figure 4.7: Various α_l and constant $L_{tot} = 80$, $\overline{E} = [10000, 10000]$, $\overline{d_0} = 0.005$

Figure 4.8 shows the influence of the aspect ratio α_l on the eigen frequencies, dimensionless wave lengths and $\Delta\theta$ RAO. Note due to the asymmetry, the mode shapes are different for each aspect ratio α_l. Figure 4.7a and 4.7b show that the first two modes are unaffected by the aspect ratio. This indicates that pure heave and rotation are governing, relative rotation does not influence these eigenfrequencies. Mode three and above are influenced by the aspect ratio. No systematic relation could be proven between the aspect ratio and the eigenfrequency and dimensionless wavelengths. In addition to this, no relation could be proven between alternative dimensionless wavelengths $\left(\frac{\alpha_l L}{\lambda}\right)$ or $\left(\frac{(1-\alpha_l)L}{\lambda}\right)$. Because the third mode is the most profitable mode for energy conversion, this is the only one that will be described. The eigenfrequency and dimensionless wavelength of the third mode increase as the aspect ratio decreases.

Table 4.3: Relation dimensionless wavelength and α_l

Aspect ratio α_l	0.1	0.2	0.3	0.4	0.5
3^{rd} [L_{tot}/λ]	2.28	1.54	1.25	1.14	1.10

Figure 4.7c shows that the relative rotation ($\Delta\theta$) decreases as the aspect ratio increases. This is supported by the goniometric relation provided in section 4.1.1 and equation (4.3). The resonance shapes corresponding to the $\Delta\theta$ RAO peaks have been decomposed into eigenmodes according to the method described in section 2.5.3. The decomposition of the resonance shapes in figure 4.8 shows that the amplitude of the third mode,

the most profitable mode for energy conversion, is maximal for an aspect ratio of $0.2 \leq \alpha_l \leq 0.3$.

From these results the following conclusions are derived:

- The aspect ratio affects the third and higher modes.
- The dimensionless wavelength of the third mode increases as the aspect ratio decreases.
- Decreasing the aspect ratio increases the relative rotation $\Delta\theta$.
- an aspect ratio of $0.2 \leq \alpha_l \leq 0.3$ results in the largest amplitude of the third in resonance.

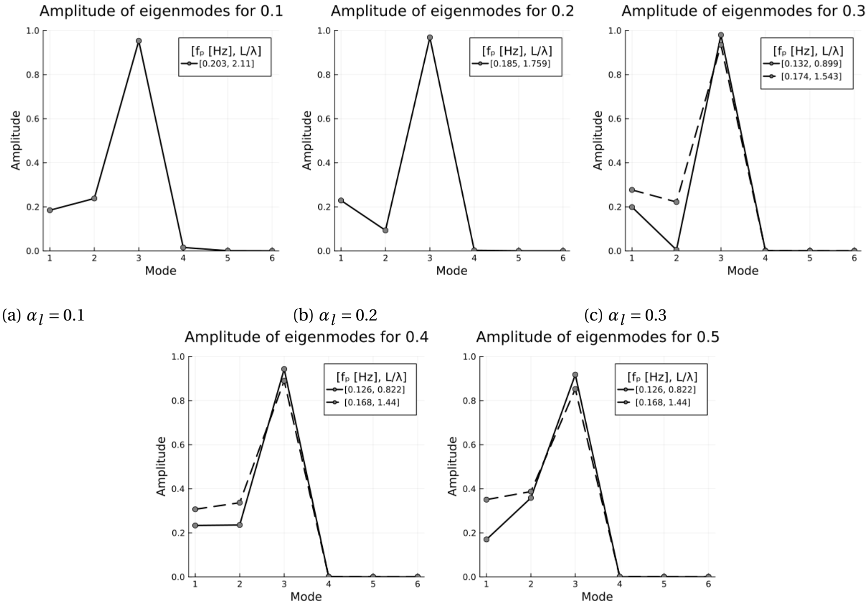

(a) $\alpha_l = 0.1$

(b) $\alpha_l = 0.2$

(c) $\alpha_l = 0.3$

(d) $\alpha_l = 0.4$

(e) $\alpha_l = 0.5$

Figure 4.8: : The modal decomposition of various resonance shapes, corresponding to peak frequencies f_p and dimensionless wavelengths $\frac{L_{tot}}{\lambda}$, for various α_l and constant $L_{tot} = 80$, $\overline{E} = [10000, 10000]$, $\overline{d_0} = 0.005$

4.1.4. Asymmetrical raft stiffness

Asymmetrical raft stiffness refers to a different dimensionless stiffness coefficient of the fore and aft raft e.g. $\overline{E}_1 \neq \overline{E}_2$. Figure 4.9 shows the eigenshapes for various asymmetrical raft stiffness.

The influence of an asymmetric raft stiffness on the eigenfrequency, dimensionless wavelength and $\Delta\theta$ RAO is shown in figure 4.10. Figure 4.10a shows the influence of the fore raft stiffness on the eigenfrequencies. Similar to what was shown in section 4.1.2 the asymmetrical stiffness does not have any influence on the eigenfrequencies of the first three modes. This confirms that these modes are governed by rigid body behaviour. For mode 4 and above figure 4.10a shows that increasing the stiffness increases the eigenfrequencies. This is in line with the relation provided in subsection 4.1.1, equation (4.2), that shows that the eigenfrequency of flexible behaviour-governed modes is proportional to the square root of the stiffness.

The $\Delta\theta$ RAO for various fore raft stiffness coefficients are shown in figure 4.10c. The $\Delta\theta$ RAO show that the peak frequencies at f = 0.126 and 0.168 are not influenced by the fore raft stiffness. However, because $\Delta\theta$ increases for higher frequency peaks they are absorbed in the $f = 0.2$ peak for very flexible fore rafts $\overline{E}_1 \leq 10$. The modal amplitudes of the resonance shapes in figure 4.11 show that resonance shapes at f = 0.126 and 0.168 consist of rigid behaviour-governed modes. This explains why their frequency is unaffected by the stiffness. Furthermore, figure 4.10c shows that the relative rotation $\Delta\theta$ increases for a lower fore raft stiffness. The modal amplitudes in figure 4.10c show that this coincides with an increase of flexible behaviour-governed modes. From this the following conclusion is derived, the relative rotation $\Delta\theta$ does not decrease for rigid

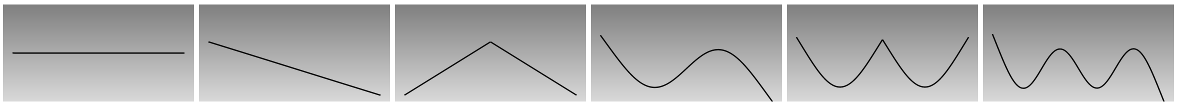

(a) $[\overline{E}_1, \overline{E}_2] = [10000, 10000]$

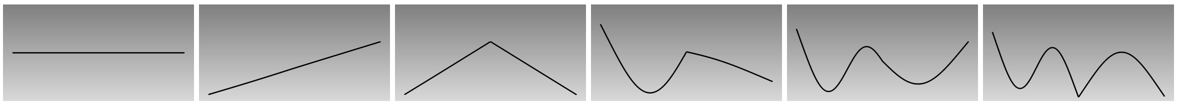

(b) $[\overline{E}_1, \overline{E}_2] = [1000, 10000]$

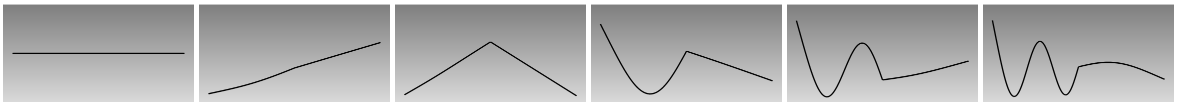

(c) $[\overline{E}_1, \overline{E}_2] = [100, 10000]$

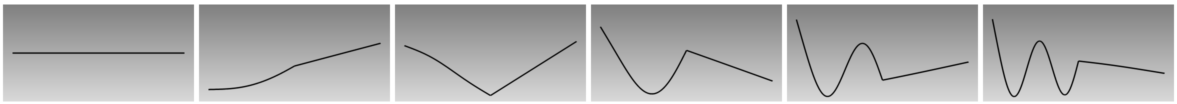

(d) $[\overline{E}_1, \overline{E}_2] = [10, 10000]$

Figure 4.9: The first six eigenshapes for various asymmetrical stiffness ratios, corresponding eigenfrequencies and dimensionless wavelengths are shown in figure 4.10,, all multiplied by an amplification factor of 100 for Various $\overline{E}_1$ and constant $L_{tot} = 80$, $\alpha_l = 0.5$, $\overline{E}_2 = 10000$, $\overline{d_0} = 0.005$

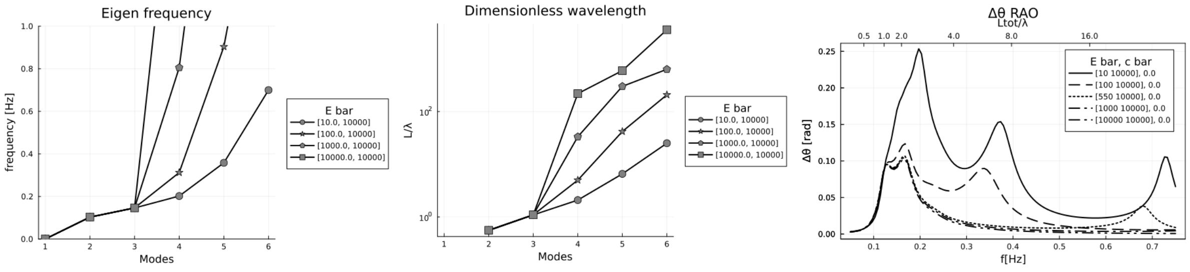

(a) Eigen frequencies for various $\overline{E}_1$

(b) $\frac{L}{\lambda} \equiv f_n$ for various $\overline{E}_1$

(c) $\Delta\theta$ RAO for various $\overline{E}_1$

Figure 4.10: Various $\overline{E}_1$ and constant $L_{tot} = 80$, $\alpha_l = 0.5$, $\overline{E}_2 = 10000$, $\overline{d_0} = 0.005$

behaviour-governed modes (1:3) but does increase for mode 4 and above for a more flexible fore raft. Finally, figure 4.10c shows the introduction of higher frequency peaks at f = 0.33, 0.37, 0.73. The modal amplitudes show that these peaks are introduced by flexible behaviour-governed modes e.g. modes 4 and above.

From these results we can derive the following conclusions:

- The first three modes are governed by rigid behaviour because the eigenfrequencies are not influenced by the asymmetric raft stiffness.
- Modes 4 and above are governed by flexible behaviour because the eigenfrequencies are influenced by the asymmetric raft stiffness.
- The eigenfrequencies and dimensionless wavelengths of mode four and above increase for increasing fore raft stiffness.
- There are more modes present per resonance shape because the eigenfrequencies move closer to each other as the fore raft stiffness decreases.
- A more flexible fore raft with constant aft raft stiffness increases the relative rotation $\Delta\theta$ for flexible behaviour-governed modes while not decreasing the relative rotation $\Delta\theta$ for rigid behaviour-governed modes.

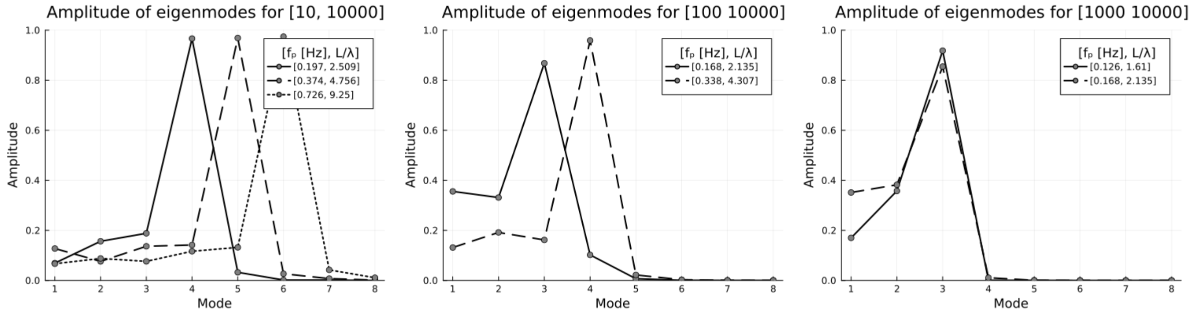

(a) $\overline{E} = [10, 10000]$ (b) $\overline{E} = [100, 10000]$ (c) $\overline{E} = [1000, 10000]$

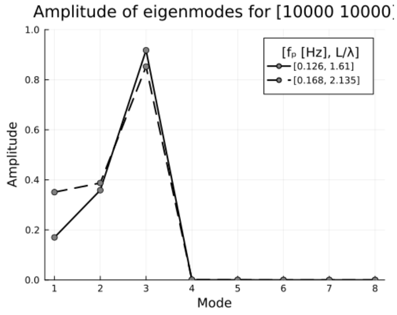

(d) $\overline{E} = [10000, 10000]$

Figure 4.11: The modal decomposition of various resonance shapes, corresponding to peak frequencies f_p and dimensionless wavelengths $\frac{L_{tot}}{\lambda}$, for various $\overline{E}_1$ and constant $L_{tot} = 80$, $\alpha_l = 0.5$, $\overline{E}_2 = 10000$, $\overline{d_0} = 0.005$

4.2. Combined WEC optimisation

This section presents the results of the combined WEC optimisation for annual energy conversion and energy stability. The figures leading to the conclusions are presented in this section, the complete results are reported in appendix A. Due to the high dependency between parameters, most parameters can only be optimised when considering combined effects. To assess the combined effects, three sets of varying parameters are tested, the total length, aspect ratio and damping coefficient $[L_{tot}, \alpha_l, \overline{c}_r]$, the symmetric stiffness, aspect ratio and damping coefficient $[\overline{E}, \alpha_l, \overline{c}_r]$ and the asymmetric stiffness and damping coefficient $[\overline{E}_1, \overline{E}_2, \overline{c}_r]$. Because the optimisation procedure described in 2.6.2 takes the wave climate into account the value of optimum parameters is site-specific. However, the underlying relations can be applied to other sites.

4.2.1. Total length, length ratio and damping coefficient

This test investigates the effects of the total length of the WEC (L_{tot}), the aspect ratio (α_l) and the corresponding optimum damping parameter c_r. This is done with a constant symmetrical stiffness of $\overline{E} = [10000, 10000]$. The section starts with the presentation of the results, followed by a discussion of the parameters per paragraph.

The optimum damping parameter for maximal annual energy conversion is obtained by the method described in subsection 2.6.2. In figure 4.12a the optimum $c_{r,opt}$ is shown in a form that contains dimension. This gives more insight into the relation between $c_{r,opt}$ and the total length, which can be well estimated by a third-order polynomial. Figure 4.12b shows the converted energy for $L_{tot}$and α_l with the optimum damping parameter, this relation has been normalised in figure 4.12c. The data in figures 4.12b and 4.12c is represented as a contour plot in figure A.2. Finally, the capture width is displayed in figure 4.13 for L_{tot} = [60, 80, 100] which are the optimum lengths for various aspect ratios according to the normalised yearly energy production shown in figure 4.12c.

Damping parameter

The optimum damping parameter for maximal annual energy conversion is an equilibrium of extracting as much energy, without suppressing the motion excessively. The influence of the optimum damping parameter in relation to the total length and aspect ratio can be summarised as follows. The forcing moment is caused

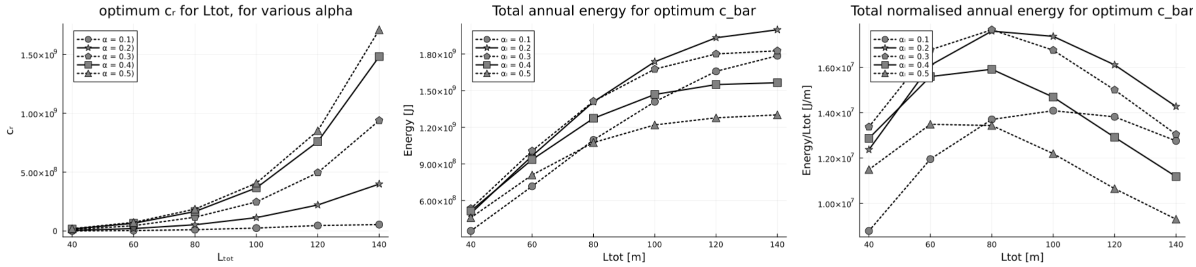

(a) The optimum damping parameter c_r

(b) Annual energy conversion for variable L_{tot},α_l and respective optimum c_r

(c) Normalised annual energy conversion for variable L_{tot},α_l and respective optimum c_r

Figure 4.12: Optimum damping parameter, annual energy conversion and normalised annual energy conversion for various α and L_{tot}

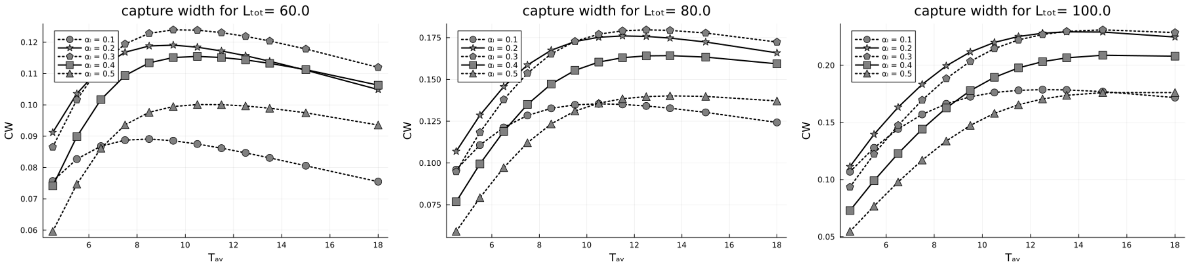

(a) Total length L_{tot} = 60

(b) Total length L_{tot} = 80

(c) Total length L_{tot} = 100

Figure 4.13: Capture width over the mean zero crossing period for various α and L_{tot}

by the hydrostatic stiffness, and the momentum of the water, both scaled by raft length. Therefore, short rafts favour a low damping parameter as they have a small forcing moment. Large raft lengths have a large forcing moment, favouring a larger damping parameter. The influence of the damping parameter on the behaviour of the WEC can be observed in figure 4.14. Figure 4.14a shows the relative rotation for the undamped WEC, figure 4.14b shows the relative rotation for the damped WEC, and finally figure 4.14c shows the power for the damped WEC.

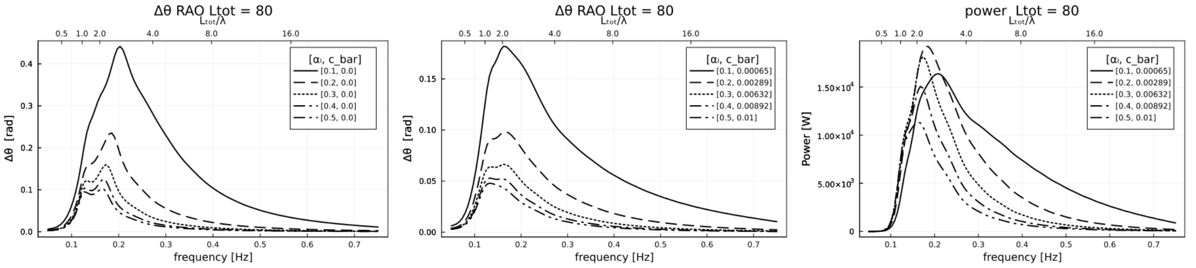

(a) The $\Delta\theta$ RAO, excluding PTO damping

(b) The $\Delta\theta$ RAO, including PTO damping

(c) The power spectrum, including PTO damping

Figure 4.14: The undamped $\Delta\theta$ RAO, damped $\Delta\theta$ RAO and damped power spectrum for variable aspect ratio

Total length

The total length describes the length of the fore and aft raft combined. The effects of total length and aspect ratio on annual energy conversion are shown in figure 4.12b. Increasing the length of the WEC has two effects on energy conversion. Firstly, increasing the length allows the WEC to extract energy over a longer distance. Secondly, increasing the length reduces the eigenfrequencies and corresponding dimensionless wavelengths, which allows resonance to occur at lower frequencies.

The converted energy is normalised by the total length, this eliminates the influence of a longer energy extraction length described previously. Figure 4.12c shows the normalised annual energy. The maximum normalised annual energy is obtained for WECs of 80m. Most energy can be extracted from the third eigenmode, which is the lowest eigenmode that results in relative rotation, while minimum energy is lost on bending the rafts. Section 4.1.1 has shown that for this mode the dimensionless wavelength is approximately equal to 1.1 for all WEC lengths. Therefore, the most important parameter is the wavelength. The annual significant wave period is determined by superpositioning the energy density spectra for the wave scatter data in figure 2.4. The annual significant period, corresponding wavelength and resulting optimum total WEC length is presented.

$$T_s = 6.61s \qquad \lambda_s = 68.1\text{m}$$

Using equation (4.4):

$$L_{tot,opt} = \left(\frac{L_{tot}}{\lambda}\right)_3 * \lambda_s \tag{4.4}$$

$$\left(\frac{L_{tot}}{\lambda}\right)_3 : \text{Dimensionless wavelength } 3^{rd} \text{ mode}$$

The relation to dimensionless wavelength of the third mode explains why for an aspect ratio of $\alpha_l = 0.5$, total lengths of 60m and 80m perform best. Furthermore, the increase in optimal total length in figure 4.12c is explained by section 4.1.3, table 4.3, which showed that the dimensionless wavelength increases when reducing the aspect ratio. The discrepancy between the resultant $L_{tot,opt}$ due to values in table 4.3 and $L_{tot,opt}$ in figure 4.12c is due to the neglect of added mass, see subsections 2.5.2 and 4.1.1 for elaboration. Besides, the capture width per zero mean crossing period, hence the energy stability is not significantly affected by total length.

Aspect ratio

The aspect ratio refers to the ratio of the fore raft length and the total length. Figure 4.12b shows that, except for very small aspect ratios $\alpha_l < 0.2$, smaller aspect ratios lead to larger annual energy conversion. This is supported by the capture width shown in figure 4.13, which shows that a small aspect ratio leads to a more evenly distributed capture width, and therefore a larger energy stability. Most notable is the capture width of a WEC of 80m, with alpha 0.2 vs 0.3. Both aspect ratios convert the same energy annually, however, an aspect ratio of 0.2 provides a more stable power source. This is explained by figure 4.14a, which shows that reducing the aspect ratio up to $\alpha_l = 0.2$ does not influence the power absorption at lower frequencies (f<0.13), but significantly increases power absorption for higher frequencies (f>0.13).

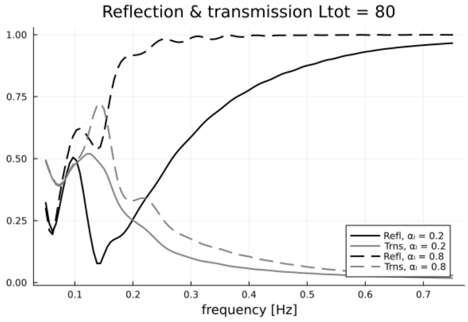

Figure 4.15: Reflection and transmission coefficients for conjugate forms of aspect ratio

The increased power absorption of WECs with a low aspect ratio for higher frequencies is due to the reduced reflection. Waves with a wavelength shorter than the raft are reflected by the raft. By applying a smaller aspect ratio, these wavelengths are not reflected by the fore-raft, without compromising the absorption of larger waves, as these can be absorbed by the aft raft. This is shown in figure 4.15, which shows the conjugate pairs of $\alpha_l = 0.2$ and $\alpha_l = 0.8$. The figure shows that the reflection for small aspect ratios is significantly smaller, whereas the transmission coefficient is similar. Note that the reflection coefficient is calculated by the difference of surface elevation and incident wave height, and contains both reflection and radiation. In addition to this a minor contribution to the increased energy conversion is due to the increase of the amplitude of the third mode for an aspect ratio of 0.2 or 0.3, see section 4.1.3.

4.2.2. Total length, symmetric raft stiffness and damping coefficient

This test investigated the effects of total length of the WEC (L_{tot}), the symmetrical stiffness $\overline{E}$ and the corresponding optimum damping parameter c_r. The aspect ratio is constant for this test, $\alpha_l = 0.5$. The optimum damping parameter for maximal annual energy conversion is obtained by the method described in 2.6.2. In figure 4.16a the optimum $c_{r,opt}$ is shown. The PTO damping parameter is shown in the form containing dimension because this gives more insight into the relation between $c_{r,opt}$ and the total length. Figures 4.16b and 4.16c show the annual energy conversion and normalised annual energy conversion for the optimum damping parameter. The data in figures 4.16b and 4.16c is represented as a contour plot in figure A.6. The section starts with the presentation of the results, followed by a discussion of the parameters per paragraph.

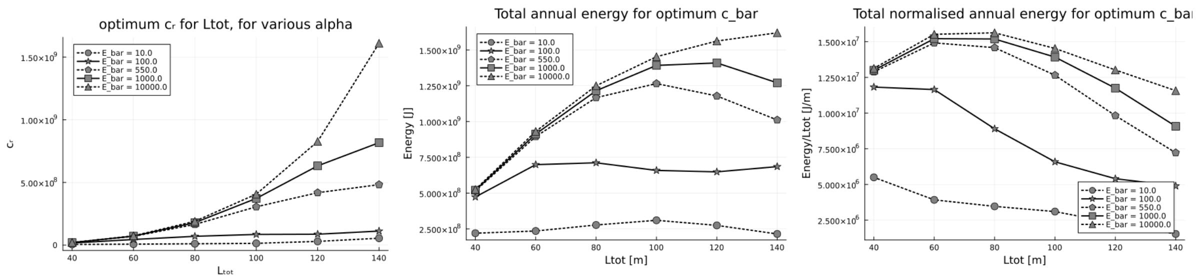

(a) Optimum damping parameter c_r

(b) Annual energy conversion for variable L_{tot}, symmetric $\overline{E}$ and respective optimum c_r

(c) Normalised annual energy conversion for variable L_{tot}, symmetric $\overline{E}$ and respective optimum c_r

Figure 4.16: Optimum damping parameter, annual energy conversion and normalised annual energy conversion for various total lengths, and symmetric raft stiffness

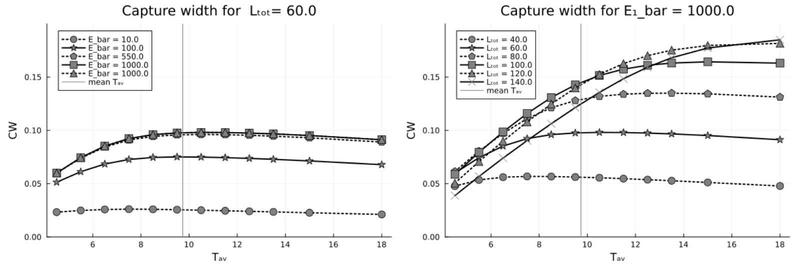

(a)

(b)

Figure 4.17: Capture width over the mean zero crossing period for various total lengths, and symmetric raft stiffness

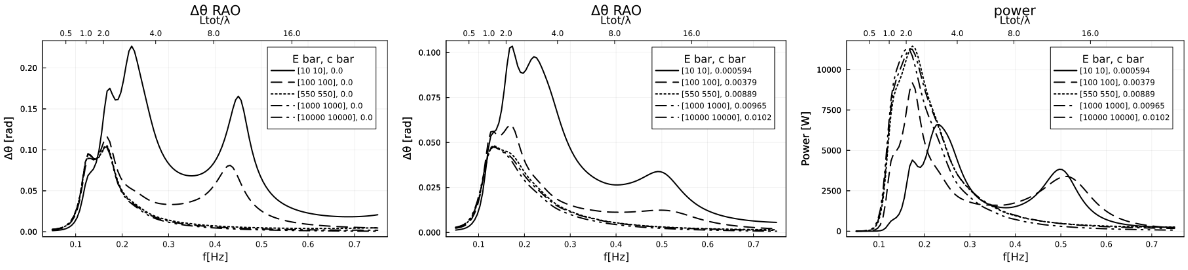

(a) The $\Delta\theta$ RAO, excluding PTO damping

(b) The $\Delta\theta$ RAO, including PTO damping

(c) The power spectrum, including PTO damping

Figure 4.18: The undamped $\Delta\theta$ RAO, damped $\Delta\theta$ RAO and damped power spectrum for variable symmetric raft stiffness

Damping parameter

The optimum damping parameter for maximal annual energy conversion is shown in 4.16a. Note that As the stiffness decreases the $c_{r,opt}$ deviates from the polynomial shown in 4.2.1. The lower the stiffness, the lower L_{tot} at which the deviation starts to occur. By reducing the raft stiffness, displacement of the raft is absorbed by bending, resulting in less moment transfer to the PTO joint for the third mode, see equation (4.5).

$$M \propto \sqrt{\eta}\frac{EI}{L} \tag{4.5}$$

This results in a lower optimum damping parameter. The influence of the damping parameter on the relative rotation $\Delta\theta$ is shown in figure 4.18.

Symmetric raft stiffness
The effect of raft stiffness on the annual energy conversion is shown in figures 4.16b and 4.16c. Reducing the raft stiffness decreases the optimum total WEC length. When the stiffness of the raft decreases, displacement will be absorbed by bending the raft, which results in less moment transfer to the PTO joint, which was shown in equation (4.5). This effect is amplified by the raft length. In addition to this figures 4.16b and 4.16c show that a lower stiffness leads to lower annual energy conversion. This is due to the low moment transfer which requires a lower optimum PTO damping parameter. The result of this is shown in figure 4.18, which shows that reducing the stiffness leads to a low power absorption at $f_p \approx 0.13$ of the third mode.

Figure 4.17a shows the influence of the symmetrical stiffness on the capture width of the WEC for various mean zero-crossing periods. It shows that stiff structure have a slightly less stable capture width than more flexible structures. However, for any T_{av} stiff rafts have a higher capture width than more flexible structures. This is explained by the power spectrum in figure 4.18c, which shows that within the range of probable peak periods ($0.09Hz < f_p < 0.16Hz$), symmetrical flexible structures never outperform more rigid structures. Therefore, the more stable capture width is of little significance because the power absorption will always be higher for stiffer structures.

4.2.3. Variable raft stiffness and damping coefficient

This test investigated the effects of asymmetric raft stiffness ($\overline{E}_1$, $\overline{E}_2$) and the corresponding optimum dimensionless damping coefficient ($\overline{c}_r$). The optimum damping parameter for maximal annual energy conversion is obtained by the method described in 2.6.2. Figure 4.19a shows the optimum dimensionless PTO damping parameter for various raft stiffness. Figure 4.19b shows the annual energy conversion for various stiffness combinations with their optimum damping parameter. The data in figure 4.19b is represented as a contour plot in figure A.11. The section starts with the presentation of the results, followed by a discussion of the parameters per paragraph.

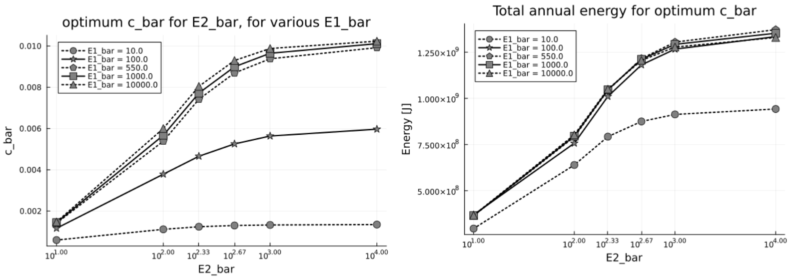

(a) Optimum dimensionless damping parameter $\overline{c}_r$

(b) Annual energy conversion for asymmetric $\overline{E}$ and respective optimum dimensionless $\overline{c}$

Figure 4.19: Optimum dimensionless damping parameter and annual energy conversion for various asymmetric raft stiffness

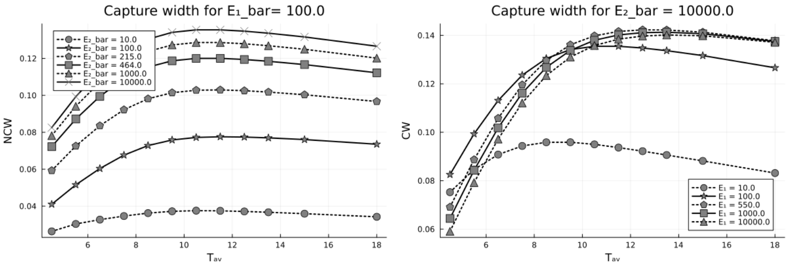

(a) Constant fore-raft stiffness, variable aft-raft stiffness $\overline{E}_1 = 100$

(b) Variable fore-raft stiffness, constant aft-raft stiffness $\overline{E}_2 = 10000$

Figure 4.20: Capture width over the mean zero crossing period for various asymmetric raft stiffness

Damping parameter

The influence of asymmetric stiffness on the optimum damping parameter for maximal annual energy conversion is shown in figure 4.19a. The figure shows that increasing either the stiffness of the fore raft or the aft raft, leads to a higher optimum damping parameter. This can be explained by the same principle provided in section 4.2.2. By reducing the raft stiffness, displacement is absorbed by bending, resulting in less moment transfer to the PTO joint for the third mode, see equation (4.5).

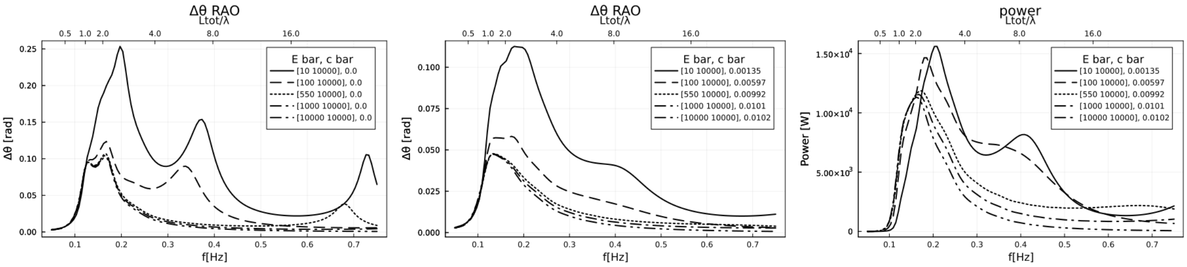

(a) The $\Delta\theta$ RAO, excluding PTO damping

(b) The $\Delta\theta$ RAO, including PTO damping

(c) The power spectrum, including PTO damping

Figure 4.21

Fore raft stiffness $\overline{E}_1$

The fore raft stiffness has a less straightforward effect than the symmetrical stiffness. Figure 4.19b shows that a flexible fore-raft ($\overline{E}_1 = 10$) performs significantly worse than others, but the performance of moderately stiff rafts, $100 \leq \overline{E}_1 \leq 10000$ is similar. In addition, the most rigid fore rafts are outperformed by $\overline{E}_1 = 550$. The poor performance of low fore raft stiffness $\overline{E}_1 < 10$ is due to the same principle of the reduced moment due to displacement described in section 4.2.2, equation (4.5). The increase in annual energy conversion for $\overline{E}_1 = 550$ is due to the increased power absorption for higher frequencies, see figure 4.21. This can be explained by the reflection and transmission coefficients. A very rigid fore-aft leads to a higher reflection of short waves of the fore-raft. Applying a slightly lower stiffness reduces the reflection while not compromising the moment resultant from the displacement at the PTO. The reflection and transmission coefficients are shown in figure 4.22. Note that the reflection coefficient is calculated by the difference of surface elevation and incident wave height, and contains both reflection and radiation. The increased power absorption for higher frequencies results in an increase in the energy stability for flexible fore-rafts, see figure 4.20b.

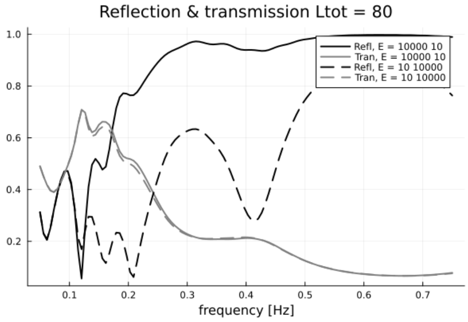

Figure 4.22: Reflection and transmission coefficients for conjugate forms of asymmetric raft stiffness

Aft raft stiffness $\overline{E}_2$

The influence of the aft raft stiffness is very similar to that of symmetrical stiffness, a stiffer aft raft leads to higher energy conversion for any stiffness of the fore-raft. A more rigid aft raft leads to higher energy absorption by the same theory provided in section 4.2.2, equation 4.5. Unlike the fore-raft stiffness, the energy absorption does not improve for a slightly flexible aft raft $100 \leq \overline{E}_2 < 10000$, because dcreasing the reflection of the aft raft does not result in a higher energy absorption because the fore-aft is excited by the reflected waves. In contrast, the adverse effects of a more flexible raft remain effective. Therefore, a stiff aft raft is beneficial

5

Conclusion

The aim of this thesis was to understand the combined effects of length, aspect ratio, raft stiffness and PTO damping on the optimisation of maximising annual energy conversion and energy stability of wave energy converters. To do this a novel formulation of a Monolithic FEM based on Timoshenko beam theory and Linear potential flow is developed. The numerical results have been verified proving a convergence rate for the mesh size equal to the polynomial order +1 and an energy-conserving model. Furthermore, the model is validated by comparing the results of the structure with and without joint to the research of Colomes et al. [32] and Khabakhpasheva et al. [31]. Furthermore, length, aspect ratio, raft stiffness and PTO damping have been optimised in a novel method maximising annual energy conversion and energy stability.

This was done by the use of two numerical experiments. Primarily, an eigenmode analysis has been performed, assessing the influence of individual parameters on eigenfrequencies corresponding to dimensionless hydraulic wavelengths and eigenmode shapes. Consequently, the real parts of complex resonance shapes of the relative rotation response amplitude operator have been decomposed in modal amplitudes. A limitation of this method is that the influence of phase difference cannot be considered.
Secondly, the length, aspect ratio, raft stiffness and PTO damping have been optimised in three sets in a combined optimisation, maximising annual energy conversion and energy stability. This was done by considering the response to 141 different JONSWAP wave spectra, dictated by significant wave height and peak period, resulting from the annual wave climate. The response has been scaled by a number of occurrences to calculate the annual energy conversion. Subsequently, the results of the optimisation have been clarified using the eigenmode analyses. A brief summary of the other results is presented in tables 5.1 and 5.2. The three most important results are:

- The optimal total length, considering raft stiffness, aspect ratio and PTO damping can be determined by matching the dimensionless wavelength corresponding to the third mode, and the annual significant wavelength.
- An aspect ratio of 0.2 to 0.3 increases the performance in high-frequency waves without compromising on low-frequency waves. The capture width is more evenly distributed over peak wave periods, indicating more energy stability. This results in an increase of annual energy conversion of 31% with respect to an aspect ratio of 0.5.
- An asymmetrical raft stiffness, with a moderately flexible fore raft and a rigid aft-raft, increases energy stability without compromising annual energy conversion.

From this, the following conclusions can be drawn. The aspect ratio is the most important parameter that can be altered to increase the annual energy conversion and energy stability. Although hydro-elasticity can improve energy stability, by increasing the capture width for high-frequency waves, it does not have a significant effect on annual energy conversion. Furthermore, there is a high dependency between all parameters and the power takeoff (PTO) damping parameter, which is why it should always be optimised to make a useful comparison of other parameters. Finally, the optimal total length is highly dependent on the significant wavelength, and the dimensionless wavelength of the third mode, confirming that this is the most profitable mode for energy conversion.

Table 5.1: Summary of results of the eigenmode analysis and RAO decomposition

Test	Result
Total length	- The dimensionless wavelength of the 2nd and 3rd mode is constant for different total lengths - The delta theta RAO peak is strongly dependent on the third mode.
Symmetric raft stiffness	- The first three modes are unaffected by stiffness, e.g. governed by rigid behaviour - Increasing the stiffness increases rotation for rigid behaviour-governed modes
Aspect ratio	- Aspect ratio of 0.2 - 0.3 maximises the amplitude of the third mode - The dimensionless wavlength of the third mode increases for decreasing aspect ratio
Asymmetric raft stiffness	- Flexible fore raft and stiff aft raft do not decrease relative rotation of rigid behaviour governed modes

Table 5.2: Summary and clarification of results of the combined parameter optimisation

Test	Result	Clarification
Total length Aspect ratio Damping	- The optimal total length, considering raft stiffness, aspect ratio and PTO damping can be determined by matching the dimensionless wavelength corresponding to the third mode, and the annual significant wavelength.	- Third mode leads to maximum relative rotation with no loss of energy on bending.
	-Total length has little effect on energy stability.	
	- Aspect ratio of 0.2 increases annual energy conversion by 31% and has a strong positive influence on energy stability.	-A small aspect ratio reduces reflection
Total length Symmetric raft stiffness Damping	- Symmetric flexibility does not improve energy conversion or energy stability, in case of symmetric stiffness.	- Flexibility leads to deflection reducing the moment due to displacement.
Asymmetric raft stiffness damping	- A moderately flexible fore raft has a positive influence on energy stability and increases annual energy conversion with 2%.	- A moderate fore raft stiffness reduces reflection while minimizing deflection resulting in a reduced moment due to displacement.
	- Flexibility of the aft raft does not improve annual energy conversion or energy stability.	- Flexibility leads to deflection reducing the moment due to displacement.

6

Recommendations

Although the model gave valuable insight into the annual energy conversion, and power stability, some phenomena could use further explanation.

Decoupling fluid and structure domains provided a useful tool to avoid singularities in the eigenvalue analysis. Furthermore, the neglect of radiation and PTO damping allowed for a real eigenvalue analysis. However, because the complex eigenshapes are not considered, information on the phase difference is lost. A phase difference between the two rafts allows for a relative rotation $\Delta\theta$ for even modes. Consequently, a complex eigenvalue analysis could provide more insight into the energy absorption capacity of even modes. In addition, the neglect of radiation damping led to overestimating the optimal dimensionless wavelength. Including damping in the eigenmode analysis could solidify the conclusion that optimum length can be determined according to the 3rd mode. Unfortunately, this could not be verified by the present tools. In addition to the inclusion of phase difference, a complex eigenvalue analysis could also provide insight into the influence of the PTO damping parameter on eigenmode shapes.

In addition to the recommendations on analysing and explaining the results, the structural properties can be optimised further. A flexible or short fore raft showed promising effects on the capture width and energy conversion. A fore-raft with variable stiffness could further exploit the principle of reducing reflection while reducing the adverse effects of lowering force transmission to the PTO system. Moreover, the model has been constructed using Timoshenko beam formulation. However, to maintain a workable number of parameters, the shear modulus has been formulated using slenderness criteria as a value dependent on Length and Young's modules, forcing the Timoshenko formulation to behave as an Euler-Bernoulli formulation. Future research could investigate the importance of shear deformation. Although stiffness was not the most influential parameter to improve performance, shear deformation increases in importance for small aspect ratios as the slenderness criteria is harder to satisfy

This report has proven that asymmetry, due to the aspect ratio or asymmetric stiffness, can improve annual energy conversion and stability. However, this asymmetry requires the WEC to be positioned directionally, so that the fore-raft is indeed ahead of the aft raft. Therefore research into a mechanism controlling the WEC orientation is required to utilise these principles.

Finally, collision was not considered in this thesis. Because the relative rotation increases for either a small aspect ratio or an asymmetric stiffness, research into the risk of collision is required to make the findings of this thesis practically applicable.

Bibliography

[1] European commision. The European Green Deal. Dec. 2019. url: `https://eur-lex.europa.eu/legal-content/EN/TXT/?qid=1588580774040&uri=CELEX%5C%3A52019DC0640`.

[2] European commision. European Green Deal: Commission proposes transformation of EU economy and society to meet climate ambitions. July 2021. url: `https://ec.europa.eu/commission/presscorner/detail/en/ip_21_3541`.

[3] A. MacGillivray et al. "Innovation and cost reduction for marine renewable energy: A learning investment sensitivity analysis". In: Technological Forecasting and Social Change 87 (2014), pp. 108–124.

[4] R. Prakash, I. K. Bhat, et al. "Energy, economics and environmental impacts of renewable energy systems". In: Renewable and sustainable energy reviews 13.9 (2009), pp. 2716–2721.

[5] S. Abbasi and N. Abbasi. "The likely adverse environmental impacts of renewable energy sources". In: Applied energy 65.1-4 (2000), pp. 121–144.

[6] K. Schmietendorf, J. Peinke, and O. Kamps. "The impact of turbulent renewable energy production on power grid stability and quality". In: The European Physical Journal B 90.11 (2017), pp. 1–6.

[7] K. Gunn and C. Stock-Williams. "Quantifying the global wave power resource". In: Renewable Energy 44 (2012), pp. 296–304. issn: 0960-1481. doi: `https://doi.org/10.1016/j.renene.2012.01.101`. url: `https://www.sciencedirect.com/science/article/pii/S0960148112001310`.

[8] A. Clément et al. "Wave energy in Europe: current status and perspectives". In: Renewable and sustainable energy reviews 6.5 (2002), pp. 405–431.

[9] B. Drew, A. R. Plummer, and M. N. Sahinkaya. "A review of wave energy converter technology". In: Proceedings of the Institution of Mechanical Engineers, Part A: Journal of Power and Energy 223.8 (2009), pp. 887–902. doi: `10.1243/09576509JPE782`. eprint: `https://doi.org/10.1243/09576509JPE782`. url: `https://doi.org/10.1243/09576509JPE782`.

[10] R. Pelc and R. M. Fujita. "Renewable energy from the ocean". In: Marine Policy 26.6 (2002), pp. 471–479.

[11] G. S. Seck et al. "Embedding power system's reliability within a long-term Energy System Optimization Model: Linking high renewable energy integration and future grid stability for France by 2050". In: Applied Energy 257 (2020), p. 114037.

[12] T. Aderinto and H. Li. "Ocean wave energy converters: Status and challenges". In: Energies 11.5 (2018), p. 1250.

[13] C. D. Masters, D. H. Root, and W. D. Dietzman. "Distribution and quantitative assessment of world crude-oil reserves and resources". In: The Changing Carbon Cycle. Springer, 1986, pp. 491–507.

[14] P. Haren. "Optimal design of Hagen-Cockerall raft". PhD thesis. Massachusetts Institute of Technology, 1979.

[15] S.-M. Zheng et al. "Numerical study on the dynamics of a two-raft wave energy conversion device". In: Journal of Fluids and Structures 58 (2015), pp. 271–290.

[16] S. Zheng and Y. Zhang. "Analytical study on hydrodynamic performance of a raft-type wave power device". In: Journal of Marine Science and Technology 22.4 (2017), pp. 620–632.

[17] D. Lu et al. "Combined effects of raft length ratio and structural flexibility on power capture performance of an interconnected-two-raft wave energy converter". In: Ocean Engineering 177 (2019), pp. 12–28.

[18] D. Lu et al. "A method to estimate the hydroelastic behaviour of VLFS based on multi-rigid-body dynamics and beam bending". In: Ships and Offshore Structures 14.4 (2016), pp. 354–362.

[19] X. Zhang et al. "The maximum wave energy conversion by two interconnected floaters: Effects of structural flexibility". In: Applied Ocean Research 71 (2018), pp. 34–47.

[20] Y. Fu and H. Ruan. “Dynamical modeling and parametric analysis of an electret-based wave energy converter”. In: International Journal of Mechanical Sciences (2022), p. 108049.

[21] S. Badia and F. Verdugo. “Gridap: An extensible Finite Element toolbox in Julia”. In: Journal of Open Source Software 5.52 (2020), p. 2520. doi: `10.21105/joss.02520`. url: `https://doi.org/10.21105/joss.02520`.

[22] F. Verdugo and S. Badia. “The software design of Gridap: A Finite Element package based on the Julia JIT compiler”. In: Computer Physics Communications 276 (July 2022), p. 108341. doi: `10.1016/j.cpc.2022.108341`. url: `https://doi.org/10.1016/j.cpc.2022.108341`.

[23] M. W. Kim, W. Koo, and S. Y. Hong. “Numerical analysis of various artificial damping schemes in a three-dimensional numerical wave tank”. In: Ocean engineering 75 (2014), pp. 165–173.

[24] Y. Kim. “Artificial damping in water wave problems II: Application to wave absorption”. In: International Journal of Offshore and Polar Engineering 13.02 (2003).

[25] K. Hasselmann et al. “Measurements of wind-wave growth and swell decay during the Joint North Sea Wave Project (JONSWAP).” In: Ergaenzungsheft zur Deutschen Hydrographischen Zeitschrift, Reihe A (1973).

[26] Y. Goda. Random seas and design of maritime structures. Vol. 33. World Scientific Publishing Company, 2010.

[27] J. Goggins and W. Finnegan. “Shape optimisation of floating wave energy converters for a specified wave energy spectrum”. In: Renewable Energy 71 (2014), pp. 208–220.

[28] O. M. Mazzaretto, M. Menéndez, and H. Lobeto. “A global evaluation of the JONSWAP spectra suitability on coastal areas”. In: Ocean Engineering 266 (2022), p. 112756.

[29] N. Nordenstrøm and B. Pedersen. “Prediction of wave-induced motions and loads for catamarans”. In: Offshore Technology Conference. OnePetro. 1971.

[30] O. Colomés, F. Verdugo, and I. Akkerman. “A monolithic Finite Element formulation for the hydroelastic analysis of Very Large Floating Structures”. In: arXiv preprint arXiv:2206.12410 (2022).

[31] T. Khabakhpasheva and A. Korobkin. “Hydroelastic behaviour of compound floating plate in waves”. In: Journal of Engineering Mathematics 44.1 (2002), pp. 21–40.

[32] O. Colomes. MonolithicFEMVLFS.jl. Version 0.1.0. Apr. 2022. doi: `10.4121/19601419`. url: `https://github.com/oriolcg/MonolithicFEMVLFS.jl`.

A

Results optimisation

A.1. Total length, aspect ratio and damping coefficient

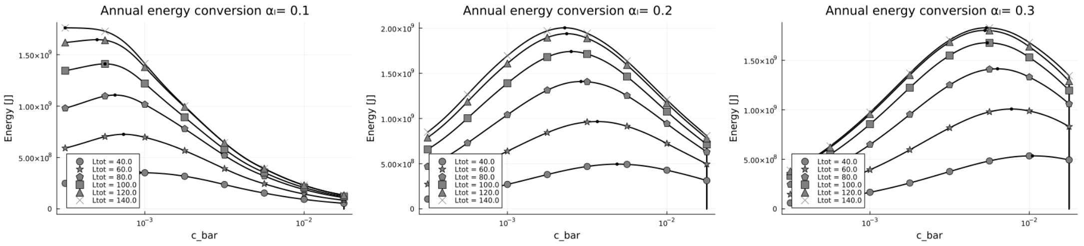

(a) Variable total lengths and damping, constant aspect ratio $\alpha_l = 0.1$

(b) Variable total lengths and damping, constant aspect ratio $\alpha_l = 0.2$

(c) Variable total lengths and damping, constant aspect ratio $\alpha_l = 0.3$

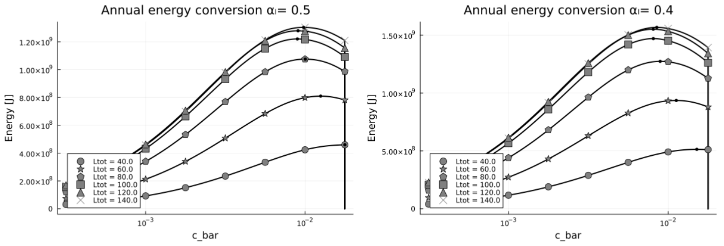

(d) Variable total lengths and damping, constant aspect ratio $\alpha_l = 0.4$

(e) Variable total lengths and damping, constant aspect ratio $\alpha_l = 0.5$

Figure A.1: Annual energy conversion for Variable total lengths, aspect ratio and damping parameter

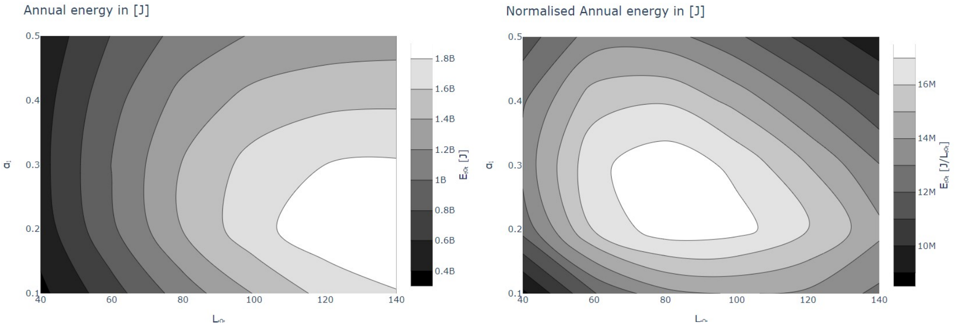

(a) Annual energy conversion

(b) Normalised annual energy conversion

Figure A.2: Contour plot of annual energy conversion and normalised annual energy conversion for Variable total length and symmetric stiffness

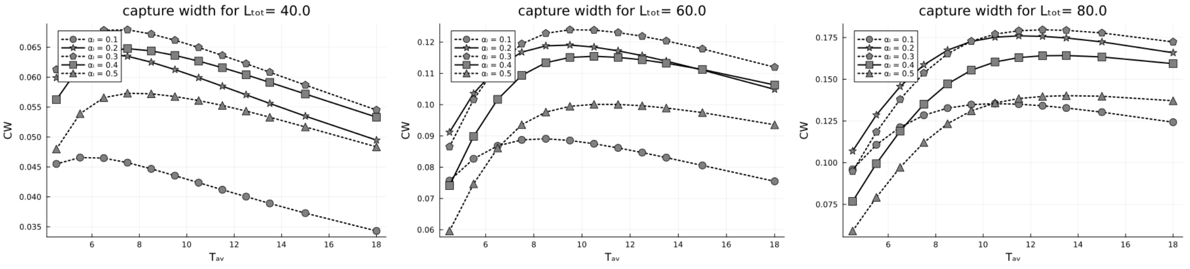

(a) Variable aspect ratio, constant total length $L_{tot} = 40$

(b) Variable aspect ratio, constant total length $L_{tot} = 60$

(c) Variable aspect ratio, constant total length $L_{tot} = 80$

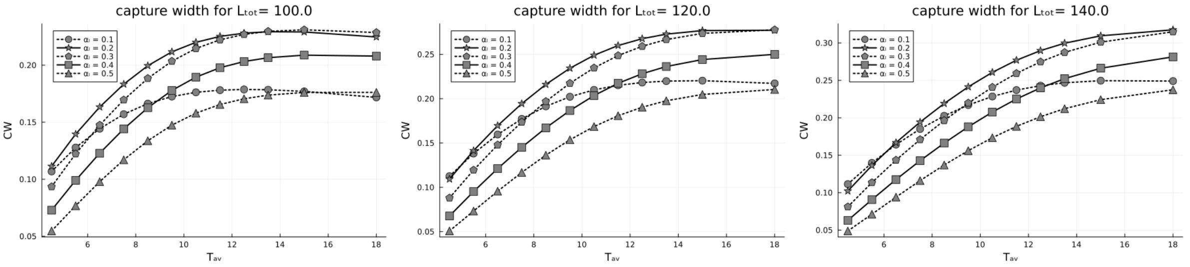

(d) Variable aspect ratio, constant total length $L_{tot} = 100$

(e) Variable aspect ratio, constant total length $L_{tot} = 120$

(f) Variable aspect ratio, constant total length $L_{tot} = 140$

Figure A.3: Capture Width over zero mean crossing period for variable total length, aspect ratio and optimum damping parameter

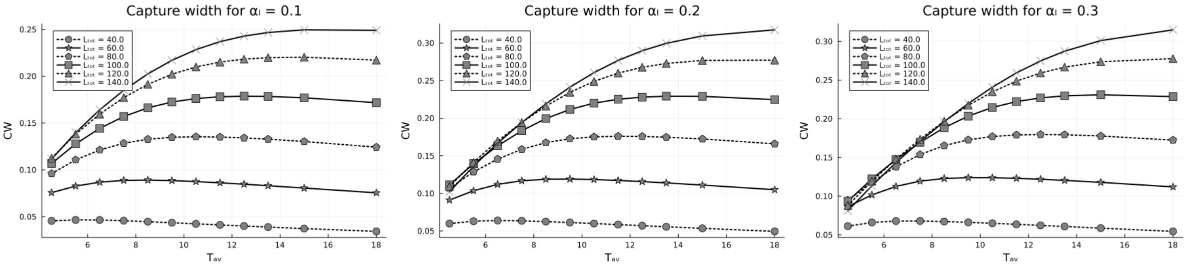

(a) Variable total length, constant aspect ratio $\alpha_l = 0.1$

(b) Variable total length, constant aspect ratio $\alpha_l = 0.2$

(c) Variable total length, constant aspect ratio $\alpha_l = 0.3$

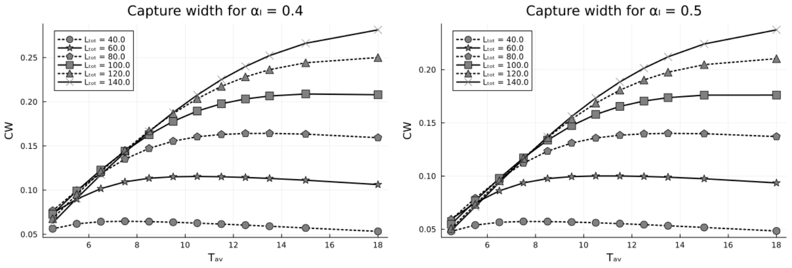

(d) Variable total length, constant aspect ratio $\alpha_l = 0.4$

(e) Variable total length, constant aspect ratio $\alpha_l = 0.5$

Figure A.4: Capture Width over zero mean crossing period for variable total length, aspect ratio and optimum damping parameter

A.2. Total length, symmetric raft stiffness and damping coefficient

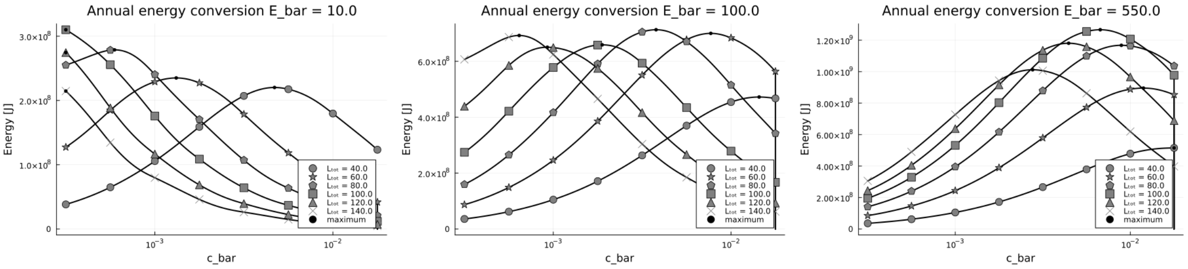

(a) Variable total lengths and damping, constant symmetric raft stiffness $\overline{E} = [10; 10]$

(b) Variable total lengths and damping, constant symmetric raft stiffness $\overline{E} = [100; 100]$

(c) Variable total lengths and damping, constant symmetric raft stiffness $\overline{E} = [550; 550]$

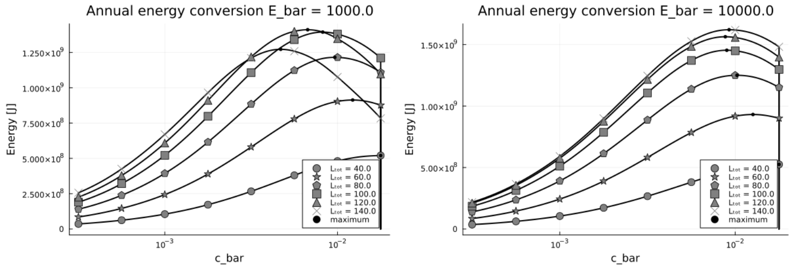

(d) Variable total lengths and damping, constant symmetric raft stiffness $\overline{E} = [1000; 1000]$

(e) Variable total lengths and damping, constant symmetric raft stiffness $\overline{E} = [10000; 10000]$

Figure A.5: Contour plot of annual energy conversion and normalised annual energy conversion for Variable total lengths, symmetric raft stiffness and damping parameter

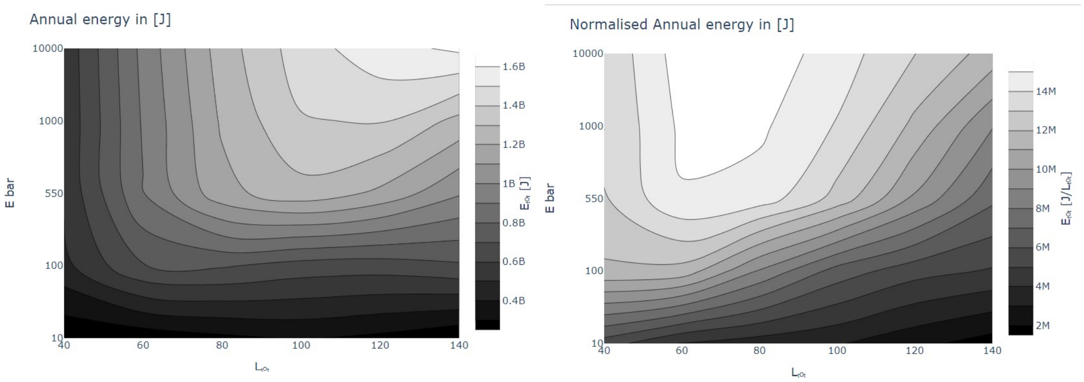

(a) Annual energy conversion

(b) Normalised annual energy conversion

Figure A.6: Contour plot of Annual energy conversion for Variable total length and symmetric stiffness, Note y-axis not the scale!

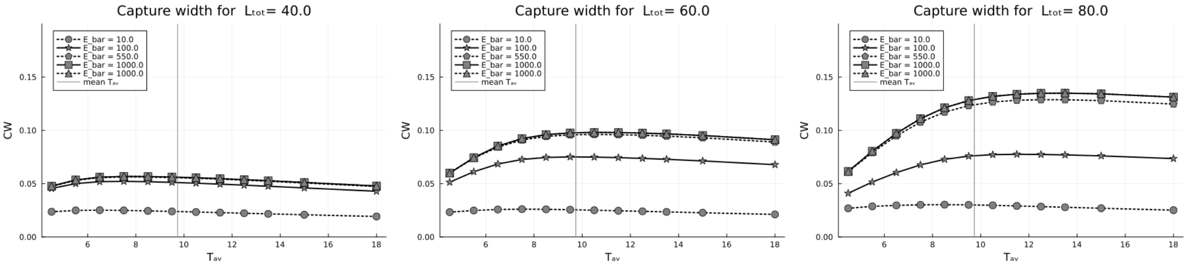

(a) Variable symmetric raft stiffness, constant total length $L_{tot} = 40$ (b) Variable symmetric raft stiffness, constant total length $L_{tot} = 60$ (c) Variable symmetric raft stiffness, constant total length $L_{tot} = 80$

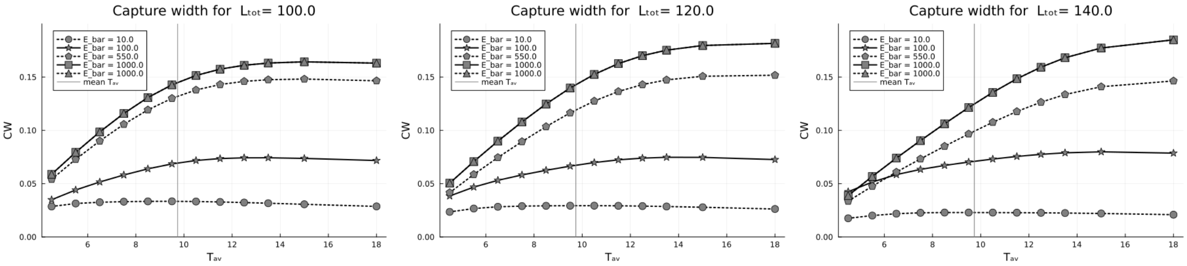

(d) Variable symmetric raft stiffness, constant total length $L_{tot} = 100$ (e) Variable symmetric raft stiffness, constant total length $L_{tot} = 120$ (f) Variable symmetric raft stiffness, constant total length $L_{tot} = 140$

Figure A.7: Capture Width over zero mean crossing period for variable total length, symmetric raft stiffness and optimum damping parameter

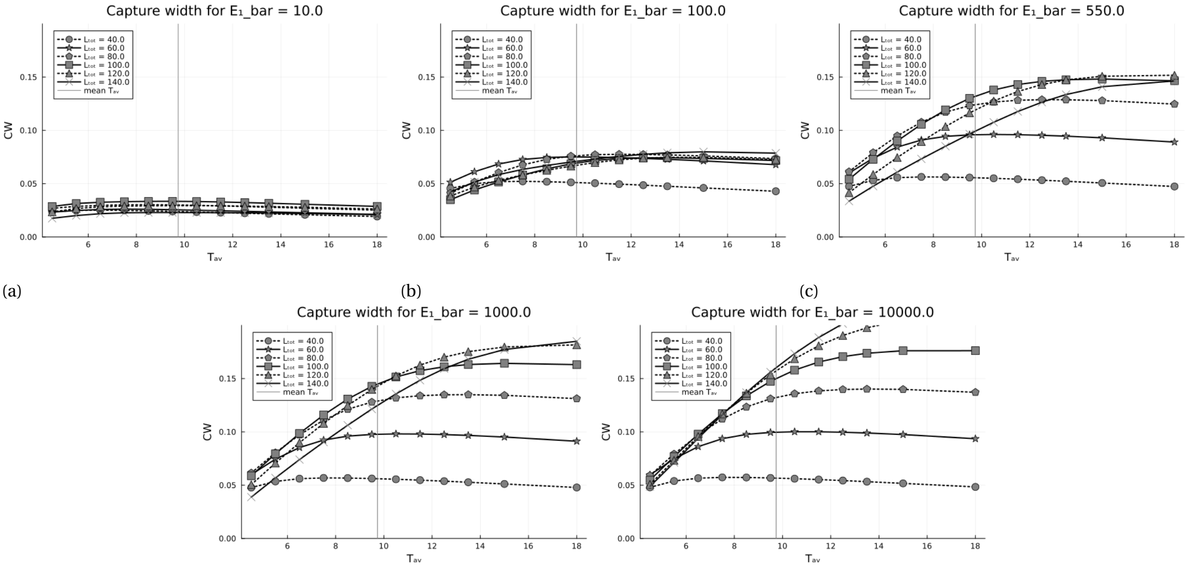

(a) (b) (c)

(d) (e)

Figure A.8: Capture Width over zero mean crossing period for variable total length, symmetric raft stiffness and optimum damping parameter

Figure A.9

A.3. Asymmetric raft stiffness and damping coefficient

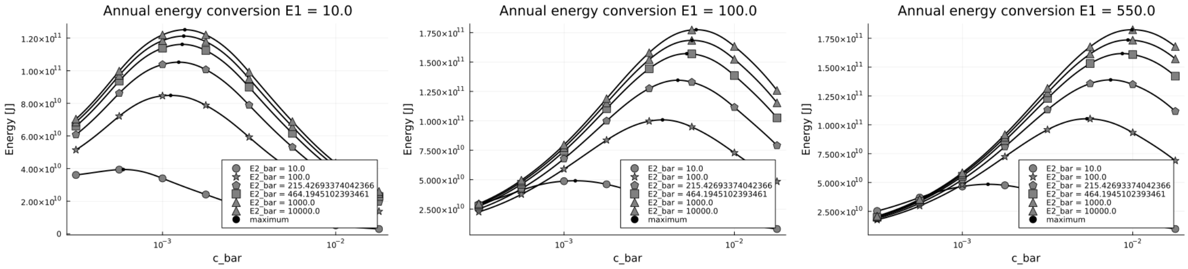

(a) Variable aft raft raft stiffness and damping, constant fore raft stiffness $\overline{E}_1 = 10$] (b) Variable aft raft raft stiffness and damping, constant fore raft stiffness $\overline{E}_1 = 100$] (c) Variable aft raft raft stiffness and damping, constant fore raft stiffness $\overline{E}_1 = 550$]

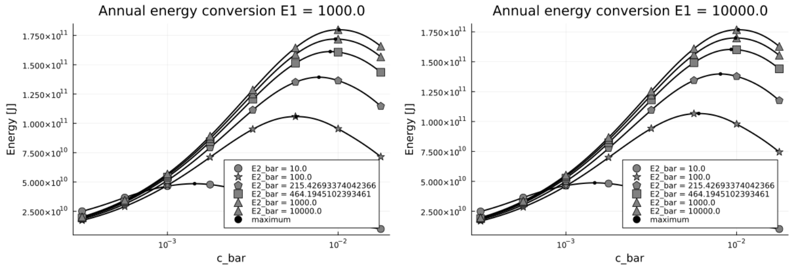

(d) Variable aft raft raft stiffness and damping, constant fore raft stiffness $\overline{E}_1 = 1000$] (e) Variable aft raft raft stiffness and damping, constant fore raft stiffness $\overline{E}_1 = 10000$]

Figure A.10: Annual energy conversion for Variable asymmetric raft stiffness and damping parameter

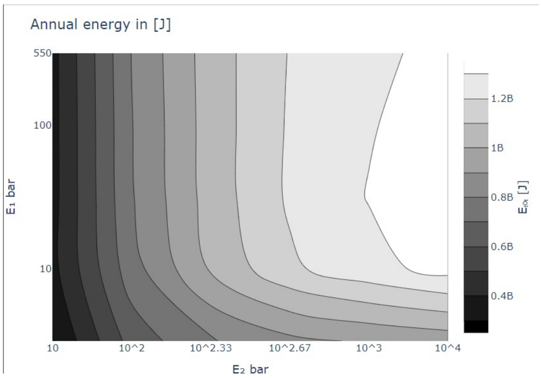

Figure A.11: Contour plot of annual energy conversion for Variable asymmetric raft stiffness and optimum damping parameter, Note x and y axis not the scale!

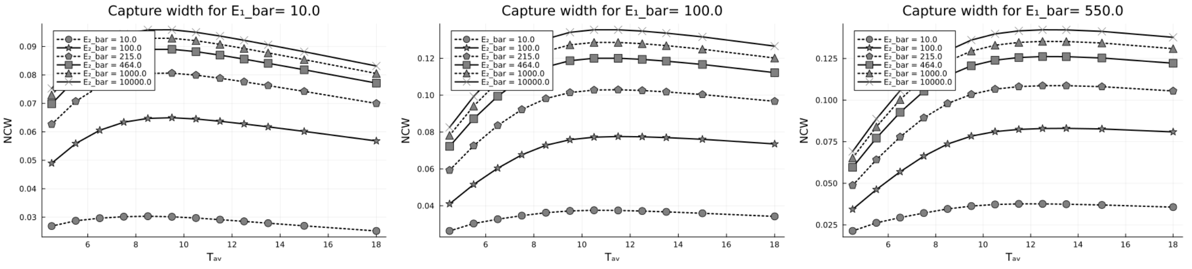

(a) Variable aft raft stiffness, constant fore raft stiffness $\overline{E}_1 = 10$ (b) Variable aft raft stiffness, constant fore raft stiffness $\overline{E}_1 = 100$ (c) Variable aft raft stiffness, constant fore raft stiffness $\overline{E}_1 = 550$

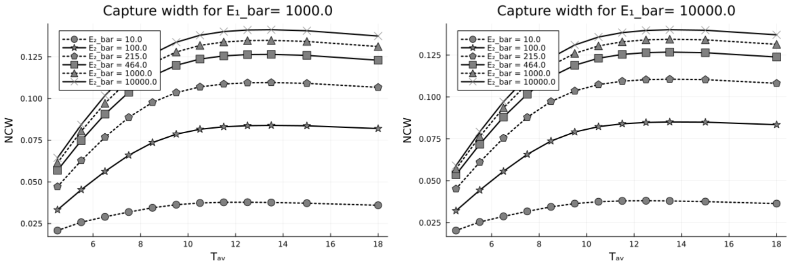

(d) Variable aft raft stiffness, constant fore raft stiffness $\overline{E}_1 = 1000$ (e) Variable aft raft stiffness, constant fore raft stiffness $\overline{E}_1 = 10000$

Figure A.12: Capture Width over zero mean crossing period for variable asymmetric raft stiffness and optimum damping parameter

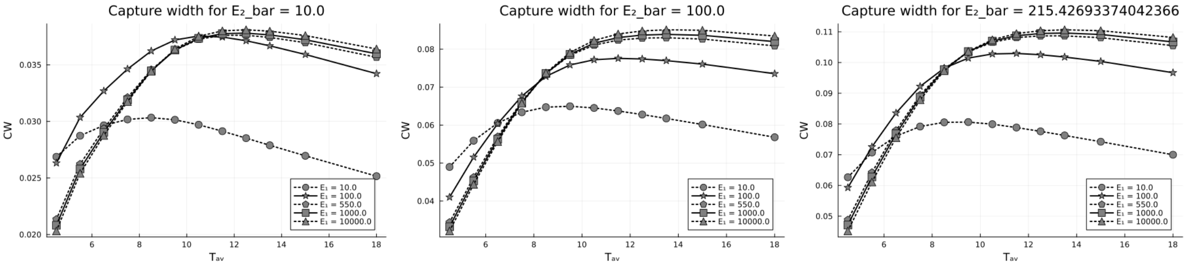

(a) Variable fore raft stiffness, constant aft raft stiffness $\overline{E}_2 = 10$ (b) Variable fore raft stiffness, constant aft raft stiffness $\overline{E}_2 = 100$ (c) Variable fore raft stiffness, constant aft raft stiffness $\overline{E}_2 = 215$

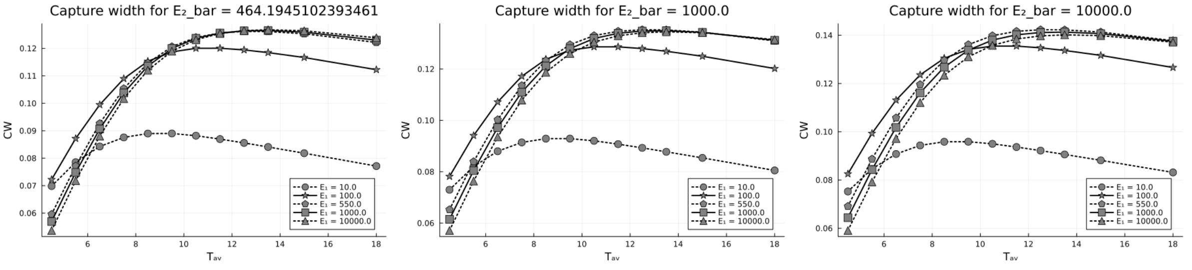

(d) Variable fore raft stiffness, constant aft raft stiffness $\overline{E}_2 = 464$ (e) Variable fore raft stiffness, constant aft raft stiffness $\overline{E}_2 = 1000$ (f) Variable fore raft stiffness, constant aft raft stiffness $\overline{E}_2 = 10000$

Figure A.13: Capture Width over zero mean crossing period for variable asymmetric raft stiffness and optimum damping parameter